Dynamics of
a model microswimmer
near a liquid-liquid interface

Chao Feng

2023

Acknowledgements

Contents

List of Publications

Chapter 2

Chao Feng, John J. Molina, Matthew S. Turner, and Ryoichi Yamamoto, "Dynamics of microswimmers near a soft penetrable interface", *Physical Review Research*, 4:043202, 2022.

This chapter is reprinted from this paper with revisions and with permission. All figures in this paper are reused in the dissertation with permission. Copyright (2022) by the American Physical Society.

Chapter 3

Chao Feng, John J. Molina, Matthew S. Turner, and Ryoichi Yamamoto, "Dynamics of microswimmers near a liquid-liquid interface with viscosity difference", *Physics of Fluids*, submitted.

Chapter 4

Chao Feng, John J. Molina, and Ryoichi Yamamoto, "Dynamics of microswimmers near a drop", in preparation.

Symbols

Symbol	Name
a	particle radius
B_n	magnitude of the Legendre polynomial of the nth order
D	distance between the center of the droplet and the swimmer
d	distance D in $\hat{\boldsymbol{x}}$ axis
$\hat{\boldsymbol{e}}$	swimming direction
$\boldsymbol{F}^C$	direct particle-particle interaction force
$\boldsymbol{F}^{ext}$	external force
$\boldsymbol{F}^H$	hydrodynamic force
I	unit tensor
$\boldsymbol{I_p}$	particle inertia moment
$\boldsymbol{J}$	particle angular momentum
L	distance between the swimmer and the interface
L_x	system width
L_z	system height
M	particle mass
m	the mth collision
$\boldsymbol{N}^C$	direct particle-particle interaction torque
$\boldsymbol{N}^{ext}$	external torque
$\boldsymbol{N}^H$	hydrodynamic torque

p	pressure
$P_n^{'}$	derivative of the Legendre polynomial of the nth order
Pe	Péclet number
$\boldsymbol{Q}$	particle orientation matrix
$\mathbb{r}$	droplet radius
$\boldsymbol{R}$	particle position
$\hat{\boldsymbol{r}}$	particle unit radial direction
Re	Reynolds number
Sc	Schmidt number
U	squirming velocity
$\boldsymbol{u}$	total velocity field
$\boldsymbol{u}_f$	fluid velocity field
$\boldsymbol{u}_p$	particle velocity field
$\hat{\boldsymbol{u}}^s$	particle surface velocity distribution
$\boldsymbol{V}$	particle velocity
$\hat{\boldsymbol{v}}$	direction of motion
w	the particles' affinity for fluid phases
$\hat{\boldsymbol{x}}$	XYZ Cartesian coordinate system of fluids system
$\hat{\boldsymbol{x}}'$	XYZ Cartesian coordinate system of swimmer body
$\hat{\boldsymbol{y}}$	XYZ Cartesian coordinate system of fluids system
$\hat{\boldsymbol{y}}'$	XYZ Cartesian coordinate system of swimmer body
$\hat{\boldsymbol{z}}$	XYZ Cartesian coordinate system of fluids system
$\hat{\boldsymbol{z}}'$	XYZ Cartesian coordinate system of swimmer body
α	coefficient of the potential energy of the interface
β	swimming type
Δ	grid spacing/unit of length
η	viscosity

η_f	fluid viscosity
η_p	particle viscosity
κ	mobility
λ	viscosity ratio
μ	chemical potential
$\boldsymbol{\Omega}$	particle angular velocity
ϕ	fluid/solid field function
φ	motion direction angle
ψ	multi-fluids field function
ρ	density
ρ_f	fluid density
ρ_p	particle density
$\boldsymbol{\sigma}$	Newtonian stress tensor
θ	swimming direction angle
ϑ	polar angle between $\hat{\boldsymbol{r}}$ and $\hat{\boldsymbol{e}}$
ξ_f	fluid-fluid interfacial thickness
ξ_p	particle–fluid interface thickness

Chapter 1

General Introduction

1.1 Microswimmers

The definition of "microswimmer" consists of two elements, "micro-" for the microscopic scale of the objects (usually less than 1mm), and "swimmer" for their means of self-propulsion through a liquid.

Prevalent examples of microswimmers in nature are bacteria and many other unicellular organisms such as *archaea*, *protozoa*, *algae*, and *fungi*. Among all bacteria, *E. coli*, which is common in human and animal intestines, is perhaps one of the most widely known and studied microorganisms. [1–7] It uses several flagella, which are rotated by a motor complex and anchored in the bacterial cell wall, to propel the bacterium. [4, 7–10] Sperm, which is closely related to the reproductive process, uses a single cilium to propel through ovary fluids and transport the male DNA to the female egg. [11–18]

For synthetic microswimmers, artificial micro- and nano-machines are gradually becoming a reality with the development of new materials and 3D printing technology or other advanced techniques. [19, 20] They show great potential in various technological and biomedical applications. [21–23] For example, they might be able to serve as the targeted

delivery of drugs or genes and other cargo to a certain target, such as a lesion, through our complex body fluid environment. [22, 24, 25]

Systematic studies on the dynamics of microswimmers are important for both biological and artificial microswimmers. These studies can help us to understand the complex behaviour of microswimmers, and thus allow us to further our understanding of basic biology. On the other hand, the related research can provide a guide for developing artificial micromachines.

1.2 Swimming at the Microscale

Swimming seems to be very easy for human beings by repeating a specific body motion to propel their body forward. However, swimming at the microscale is different from what we know about swimming in a macroscopic world. A key defining feature of microscopic swimming is the Reynolds number (Re), defined as the ratio of inertial to viscous forces,

$$\text{Re} = \frac{\text{Inertial Forces}}{\text{Viscous Forces}} = \frac{\rho U a}{\eta} \tag{1.1}$$

where ρ is the density, U is the velocity, a is a characteristic radius and η is the viscosity. If Re $>> 1$, inertial forces dominate, otherwise for Re $<< 1$, viscous forces are more influential.

In general, human swimming in water often experiences a Reynolds number in the order of 10^4, which means the swimming relies on inertia. However, for a microswimmer, Re is typically $<< 10^{-1}$, due to their very small body sizes and slow swimming velocities. That is, inertia is negligible, and viscous forces dominate.

Thus, for swimming at low Reynolds numbers, constant propulsion is needed to move consistently through the liquid due to the absence of inertia. Moreover, the motion carried out has to be non-reciprocal in order to achieve a net displacement, known as the

scallop theorem. This was first proposed by Purcell in 1977 in his famous paper "Life at low Reynolds number" [26]. Taking the motion of a scallop that can only open and closes its shell, he pointed out that the scallops in theory cannot propel themselves. However, real scallops with relatively large Reynolds numbers can swim due to the inertial force. For microorganisms such as bacteria or sperm, the non-reciprocal motion can be achieved by using their flagella or cilia [4, 7–10], whereas for the artificial microswimmers, the condition of non-reciprocality can be fulfilled through external, e.g., the magnetic field [27–29], and internal factors, e.g., distinct physical properties on Janus particle surfaces [30, 31].

1.3 Theoretical Formulations

In this chapter, we introduce the theoretical formulations that govern the dynamics of microswimmers near a liquid-liquid interface. In this dissertation, all the works are performed by means of three-dimensional direct numerical calculations with fully resolved hydrodynamics.

First of all, a numerical model for microswimmers is needed. For this, the squirmer model is applied in 1.3.1. We also discuss how to represent the different types of microswimmers theoretically with this model. Then in order to understand the hydrodynamic interactions between microswimmers and fluids, we present the Navier-Stokes equations for incompressible flow in a Newtonian fluid in 1.3.2, and the Newton–Euler equations for the dynamics of the rigid particles in 1.3.3. Due to the high calculation costs of the sharp boundaries, we introduce the Smooth Profiled Method in 1.3.4. To extend to the binary phase-separating fluid mixtures, we introduce model H by coupling the Cahn-Hillard Equations and Navier-Stokes Equations in 1.3.5.
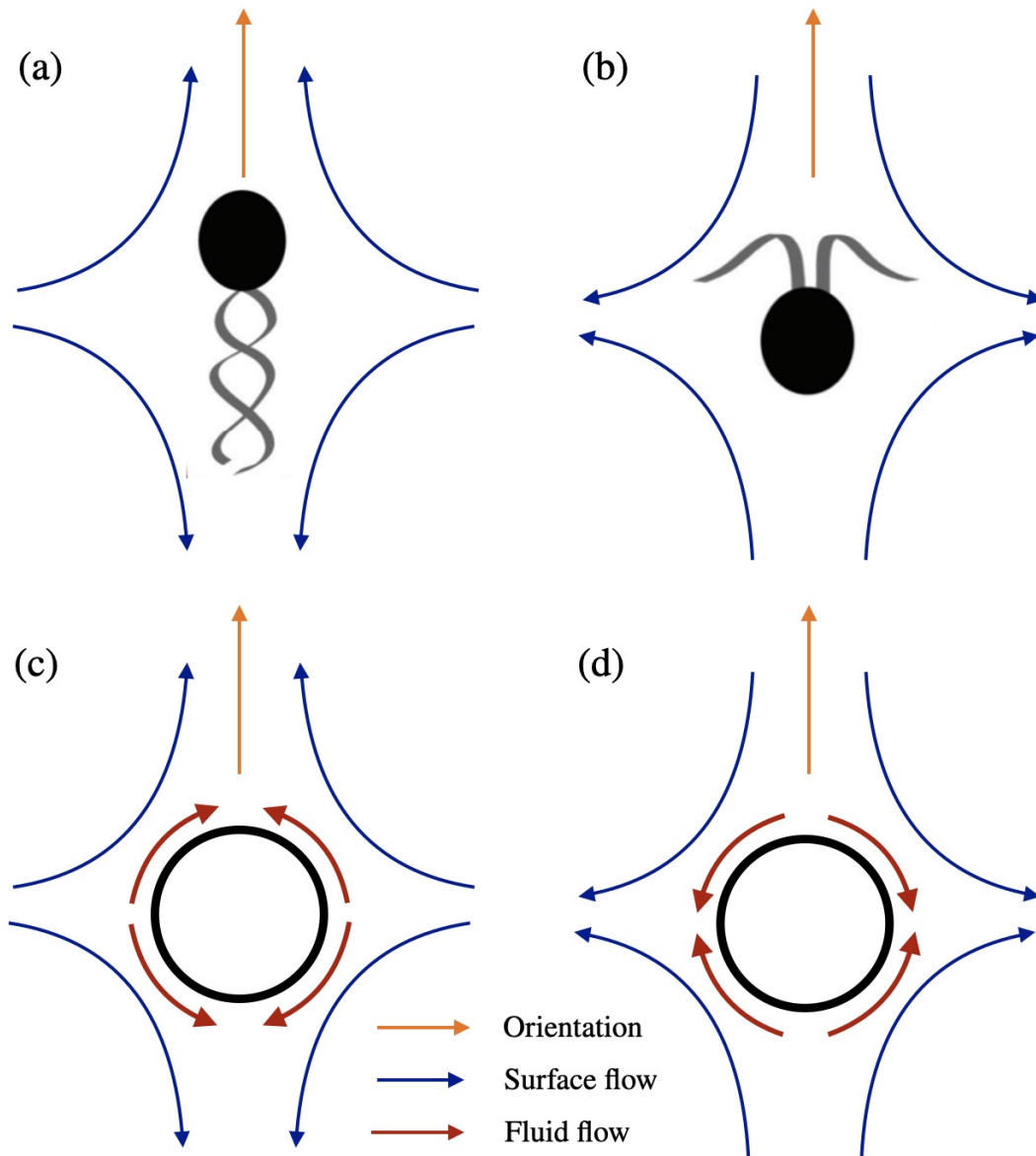
Figure 1.1. Schematic representation of the propulsion mechanism and flow profiles of a pusher and a puller (a and b), respectively. These swimmers can be represented using the squirming model, in which the detailed propulsion mechanism is replaced by a specified surface velocity at the surface of the particles for pushers and pullers (c and d), respectively.

1.3.1 The squirmer Model

For numerical analysis dynamics of the microswimmer, the squirmer model was employed in this work. This physical model is originally proposed by Lighthill [32] and later extended by Blake [33].

In this model, the irregular shape of the microswimmer is simplified to a rigid sphere, and the motion of beating cilia is represented as a distribution of velocities on its surface, as shown in Fig. 1.1. The tangential, time-independent surface velocity distribution is decomposed into a series of the form:

$$\boldsymbol{u}^s(\vartheta) = \sum_{n=1}^{\infty} \frac{2}{n(n+1)} B_n P_n^{'}(\cos\vartheta) \sin\vartheta \hat{\boldsymbol{\vartheta}}, \tag{1.2}$$

where $\vartheta = \cos^{-1}(\hat{\boldsymbol{r}} \cdot \hat{\boldsymbol{e}})$ is the polar angle between $\hat{\boldsymbol{r}}$ and the swimming direction $\hat{\boldsymbol{e}}$, $\hat{\boldsymbol{\vartheta}}$ is the unit polar angle vector, and $\hat{\boldsymbol{r}}$ is the unit vector directed from the centre of the squirmer toward a point on its surface. $P_n^{'}$ is the derivative of the Legendre polynomial of the nth order, and B_n is the magnitude of each mode. [34, 35]

Here, the activity of microswimmers is introduced in terms of the prescribed flow field. A microswimmer gives such a given flow field with respect to its own swimming direction and propels itself as the reaction of that. In this model, the assumptions are roughly only the following three: rigidity of squirmers, axisymmetry around the swimming axis, and ignorance of the components in radial or azimuthal components of the active flow field on the squirmer surfaces. Although the original derivation is done assuming a ciliary microorganism, because the assumptions are only general ones, this model can express far-field characteristics of the flow field around various types of swimmers well. This is also the case even for non-living swimmers like diffusiophoretic Janus particles.

In a Newtonian fluid, only the B_1 mode, which represents the source dipole, contributes to the steady-state propulsion velocity of the squirmer $U_0 = 2/3 B_1$, and the B_2 mode, which represents the force dipole, is physically related to the stresslet of the squirmer.

Therefore, many studies, as well as this work, considered model swimmers represented by only the first two modes of the expansion in Eq. (1.2):

$$\boldsymbol{u}^s(\vartheta) = B_1(\sin\vartheta + \frac{\beta}{2}\sin 2\vartheta)\hat{\boldsymbol{\vartheta}}, \qquad (1.3)$$

The ratio $\beta = B_2/B_1$ in Eq. (1.3) represents the swimming type of microswimmers. When β is negative, the squirmers are pushers and generate extensile flow fields along the swimming axis; When β is positive, the squirmers are pullers generating contractile flow fields. The case of $\beta = 0$ corresponds to the neutral squirmer. The main difference in the types of microswimmers can be related to the position of the propulsion mechanism along the body. A pusher is a swimmer where the propulsion is generated at the back (e.g., bacteria like *E. Coli*), while for pullers, the propulsion comes from the front (e.g., algae-like *C. Reinhardtii*). In neutral swimmers (like *Volvox*), the coefficient B_2 is small compared to B_1, and this is reflected in a symmetric flow field without vorticity.

1.3.2   The Navier-Stokes equations

The flow of liquids on macroscopic scales is governed by the Navier–Stokes equations with a constant density ρ under the incompressible condition:

$$\rho(\partial_t + \boldsymbol{u}_f \cdot \boldsymbol{\nabla})\boldsymbol{u}_f = \boldsymbol{\nabla} \cdot \boldsymbol{\sigma}, \qquad (1.4)$$

$$\boldsymbol{\nabla} \cdot \boldsymbol{u}_f = 0, \qquad (1.5)$$

where ρ is the fluid density. The Newtonian stress tensor $\boldsymbol{\sigma}$ is composed of two contributions, namely, the isotropic pressure term and the shear stress term $\boldsymbol{\sigma}_f$ due to the viscosity η:

$$\boldsymbol{\sigma} = -p\mathbf{I} + \boldsymbol{\sigma}_f, \qquad (1.6)$$

$$\boldsymbol{\sigma}_f = \eta(\boldsymbol{\nabla}\boldsymbol{u} + \boldsymbol{\nabla}\boldsymbol{u}^{\mathrm{T}}), \qquad (1.7)$$

where I is the unit tensor.

1.3.3 The Newton-Euler equations

The dynamics of the rigid particles are determined by Newton–Euler equations of motion:

$$\dot{\boldsymbol{R}}_i = \boldsymbol{V}_i, \tag{1.8}$$

$$\dot{\boldsymbol{Q}}_i = \text{skew}(\boldsymbol{\Omega}_i) \cdot \boldsymbol{Q}_i, \tag{1.9}$$

$$M_p \dot{\boldsymbol{V}}_i = \boldsymbol{F}_i^H + \boldsymbol{F}_i^C + \boldsymbol{F}_i^{ext}, \tag{1.10}$$

$$\boldsymbol{I}_p \cdot \dot{\boldsymbol{\Omega}}_i = \boldsymbol{N}_i^H + \boldsymbol{N}_i^{ext}, \tag{1.11}$$

where $M_p = \frac{4}{3}\pi a^2 \rho_p$ and $\boldsymbol{I}_p = \frac{2}{5}M_p a^2 \mathsf{I}$ are the mass and moment of inertia, respectively, of the particles with the radius a and density ρ_p; $\boldsymbol{Q}_i$ is the orientation matrix of particle i; and $\text{skew}(\boldsymbol{\Omega}_i)$ is the skew-symmetric matrix of the angular velocity $\boldsymbol{\Omega}_i$, defined as

$$\text{skew}(\boldsymbol{\Omega}) = \begin{pmatrix} 0 & -\Omega_3 & \Omega_2 \\ \Omega_3 & 0 & -\Omega_1 \\ -\Omega_2 & \Omega_1 & 0 \end{pmatrix}, \quad \boldsymbol{\Omega} = \begin{pmatrix} \Omega_1 \\ \Omega_2 \\ \Omega_3 \end{pmatrix} \tag{1.12}$$

The hydrodynamic forces and torques are given by $\boldsymbol{F}_i^H$ and $\boldsymbol{N}_i^H$, $\boldsymbol{F}_i^C$ represents direct particle–particle interactions ($\boldsymbol{N}_i^C = 0$), and $\boldsymbol{F}_i^{ext}$ and $\boldsymbol{N}_i^{ext}$ are the external forces and torques, respectively.

1.3.4 The smoothed profile method

To simulate the dynamics of a swimming system while fully considering the hydrodynamic interactions, we employ the smoothed profile (SP) method [36]. In this method, all boundaries, including both fluid/solid and fluid/fluid boundaries, are considered to possess a finite interfacial thickness ξ instead of the sharp boundary conditions which

result in very expensive calculation costs. This greatly simplifies the modelling and improves the computational efficiency of the method, as it avoids the need for complicated discretizations around the particles and the accompanying re-meshing of other direct numerical simulation (DNS) approaches, such as spectral/hp element methods[37]. Fluid/solid boundaries are implicitly accounted for by introducing a phase field function $\phi(\boldsymbol{r})$, which is equal to 1 within solid domains (inside the squirmer particles), is equal to 0 within the fluid domain (outside of the squirmer particles), and smoothly varies between 0 and 1 across the interface. Thus, such an interface can be represented by the gradient of the phase field, which will be nonzero only within the interfacial domains.

A modified (incompressible) Navier–Stokes equation is employed as the governing equation for the total fluid velocity $\boldsymbol{u}$:

$$\rho(\partial_t + \boldsymbol{u} \cdot \boldsymbol{\nabla})\boldsymbol{u} = \boldsymbol{\nabla} \cdot \boldsymbol{\sigma} + \rho(\phi\boldsymbol{f}_p + \phi\boldsymbol{f}_{sq}), \tag{1.13}$$

$$\boldsymbol{\nabla} \cdot \boldsymbol{u} = 0, \tag{1.14}$$

where $\boldsymbol{\sigma}$ is the Newtonian stress tensor (viscosity η) and ρ is the fluid density. The term $\phi\boldsymbol{f}_p$ appearing on the right-hand side of Eq. (1.13) is introduced to enforce the rigidity of the particles; likewise, the term $\phi\boldsymbol{f}_{sq}$ is introduced to enforce the "squirming" boundary condition at the surfaces of the particles (Eq. (1.3)).

The total velocity is defined in terms of the fluid velocity field $\boldsymbol{u}_f$ and the particle velocity field $\boldsymbol{u}_p$ as

$$\boldsymbol{u} = (1 - \phi)\boldsymbol{u}_f + \phi\boldsymbol{u}_p, \tag{1.15}$$

$$\phi\boldsymbol{u}_p = \sum_i \phi_i[\boldsymbol{V}_i + \boldsymbol{\Omega}_i \times \boldsymbol{R}_i], \tag{1.16}$$

where the first term, $(1 - \phi)\boldsymbol{u}_f$, represents the velocity field of the binary fluid, while the second term, $\phi\boldsymbol{u}_p$, represents the particles' velocity field, which is defined in terms

of the positions $\boldsymbol{R}_i$, velocities $\boldsymbol{V}_i$, and angular velocities $\boldsymbol{\Omega}_i$ of the particles (where i is the particle index).

The accuracy of the SP method has been extensively studied in previous work [36, 38–41]. For example, the friction and mobility tensors of non-spherical particle assemblies obtained from simulations at low Reynolds number (Re) are within $\lesssim 5\%$ of experimental values and high-precision solutions of the Stokes equation [40]. A similar degree of accuracy is found for the angular velocities of spherical particles under shear flow for $\text{Re} \lesssim 10$ [42] and the ζ potential of charged colloidal dispersions [43]. Likewise, simulation results for the terminal velocity of a rising droplet in a binary fluid (density ratio $\rho_A/\rho_B \leq 1$) were within $\lesssim 8\%$ of the theoretical predictions [41]. Finally, we note that these benchmark simulations were performed using relatively coarse resolutions, for particles of size $a = 4 \sim 5\Delta$, with interfacial thickness $\xi = 2\Delta$ (Δ the grid spacing).

1.3.5 Phase-separating dynamics

The host fluid in our system is modelled as a phase-separating binary fluid mixture using the Cahn-Hilliard (CH) model, which, coupled with the Navier-Stokes hydrodynamics, yields the so-called model H [44, 45]. The order parameters for the A and B phases, $\psi_A(\mathbf{r})$ and $\psi_B(\boldsymbol{r})$, represent the volume fractions of the constituent components ($0 \leqslant \psi_\alpha \leqslant 1$). Furthermore, since the sum total of the volume fraction of all components (fluids and particles) is constrained to be unity,

$$\psi_A + \psi_B + \phi = 1, \tag{1.17}$$

the composition of the A/B phase-separating fluid can be described in terms of a single order parameter $\psi(\boldsymbol{r})$,

$$\psi = \psi_A - \psi_B. \tag{1.18}$$

This order parameter $\psi(\boldsymbol{r})$ is defined to be equal to 1 in the A domain and -1 in the B domain.

The dynamics for $\psi(\boldsymbol{r})$ is determined by the following modified Cahn-Hilliard equation

$$\frac{\partial \psi}{\partial t} + (\boldsymbol{u} \cdot \boldsymbol{\nabla})\psi = \kappa \nabla^2 \mu_\psi, \tag{1.19}$$

where $\boldsymbol{u}$ is the total velocity field, κ is the mobility coefficient, and $\mu_\psi = \delta \mathcal{F}/\delta \psi$ is the chemical potential associated with the order parameter ψ. In what follows we will also need to account for the fluid-particle interactions using a second chemical potential associated with the ϕ order parameter, $\mu_\phi = \delta \mathcal{F}/\delta \phi$. These chemical potentials are derived from the Ginzburg-Landau free energy functional

$$\mathcal{F}[\psi, \phi] = \int d\boldsymbol{r} \left[f(\psi) + \frac{\alpha}{2}(\boldsymbol{\nabla}\psi)^2 + w\xi_p \psi (\boldsymbol{\nabla}\phi)^2 \right] \tag{1.20}$$

The first term in the integrand of Eq. (1.20), $f(\psi) = \frac{1}{4}\psi^4 - \frac{1}{2}\psi^2$ represents the Landau double-well potential, with two minima at $\psi = 1$ and -1. The second term is the potential energy associated with the fluid A/B interface, the third term represents the particles' affinity for each of the fluid A/B phases. The chemical potentials corresponding to this free-energy function are then

$$\mu_\psi = f'(\psi) + \alpha \nabla^2 \psi + w\xi_p (\boldsymbol{\nabla}\phi)^2 \tag{1.21}$$

$$\mu_\phi = 2w\xi_p (\boldsymbol{\nabla}\psi \cdot \boldsymbol{\nabla}\phi + \psi \nabla^2 \phi). \tag{1.22}$$

In what follows we assume that the particles will interact with the interface hydrodynamically but not chemically and so we set $w = 0$ in all the simulations reported below.

1.4 Thesis Objectives

The dynamics of microswimmers in a complex fluid system are studied by means of direct numerical simulation with fully resolved hydrodynamics. Our objective is clearly and consistently, that is, to investigate the dynamics of particles near the liquid-liquid interface by developing and improving the swimmer/fluids model. As a result, we have developed the relevant physical model in **Chapter 2** and added new variables and constraints in **Chapter 3** and **Chapter 4**. This dissertation is organized as follows.

In **Chapter 2**, the dynamics of microswimmers near a soft penetrable interface are investigated. Previous numerical studies of swimmer dynamics at interfaces have usually considered only far-field hydrodynamics or non-penetrable surfaces. In this chapter, a physical model in which swimmers interact with a soft, deformable, and penetrable interface is proposed to study the dynamics of microswimmers near such an interface. It is shown that microswimmers have different swimming motions after approaching the interface. The effects of the microswimmer's angle of approach, swimming types, and swim strength on the choice of swimming motion are further explored. Furthermore, by quantifying the time evolution of the orientation angle of microswimmers during a collision with the interface, the author provides the rules for change in angle for different types of microswimmers. This study also shows that microswimmers have a final stable state which is only related to their swimming strength after repeated collisions with the interface and elucidates the mechanisms involved.

Chapter 3 discusses the dynamics of microswimmers near a liquid-liquid interface with viscosity difference. In this study, the viscosity of the fluid was introduced into the binary fluid model proposed above as a phase-dependent function to analyze the dynamics of swimmers approaching a fluid-fluid interface between phase-separated fluids which have distinct viscosities. The results show that the viscosity ratio also has an effect on the movement patterns of microswimmers. By performing simulations with different viscosity ratios, the microswimmers exhibit a preference for the lower viscosity fluid.

Furthermore, strong pullers initially located in relatively low viscosity fluids are observed to swim parallel to the with a certain distance, named as "hovering" motion, which is highly consistent with previous studies on the dynamics of microswimmers near solid walls.

In **Chapter 4**, dynamics of a model microswimmer near a liquid droplet with a penetrable interface are presented. In this chapter, the study was extended from planar interfaces to non-planar surfaces. It was found that the dynamics of swimmers near the drop surface remained consistent with previous studies near a flat interface. The radius of the droplet can have a further influence on the choice of swimming modes. Additionally, in this chapter, the dependence of the critical capture radius of the droplet on the properties of the microswimmers, such as swimming types and strength, is investigated. The results show that only a strong puller is able to slide on the droplet surface. The dependency of the viscosity ratio is further studied. Compared to isoviscous systems, non-isoviscous fluids systems, both with positive and negative viscosity differences, have a negative effect on droplet capture.

In **Chapter 5**, the general conclusion is stated. The contents of this dissertation are summarized and the perspectives are presented.

Chapter 2

Dynamics of microswimmers near a soft penetrable interface

2.1 Introduction

Microswimmers, including flagellated bacteria, such as *E. coli* [9] and motile, single-celled eukaryotes, such as *Chlamydomonas* [46], are common in biology and usually exist in complex fluid environments in nature. Systematic studies on the dynamics of microswimmers that can help us to understand their complex behaviours will, thus, allow us to further our understanding of basic biology and provide a guide for developing artificial micromachines. The latter could have great potential in various technological and biomedical applications [4, 47], such as targeted drug delivery [48] or therapies using microrobots [49].

Although biological microswimmers are usually found in complex or complex fluids, most theoretical/simulation studies on their dynamics have focused on simple homogeneous host environments [50–52]. Among the few works that have focused on the dynamics of microswimmers in complex multiple-fluid systems, studies have usually focused on swimmers in the vicinity of solid/fluid interfaces [53–56] or liquid/gas interfaces [57].

These previous studies have revealed that microswimmers can be strongly influenced by liquid/solid and liquid/gas boundaries; they may loiter near, escape from, or glide along the boundary [54]. Over a longer time scale, circular motion at the boundary has even been observed with the swimming orientation determined by the boundary conditions [55].

Studies of swimmer dynamics in complex fluids systems, with soft and/or penetrable interfaces, are still limited in number due to the high associated computational costs [58, 59]. In the present chapter, we take a step toward understanding the behavior of microswimmers in complex environments by performing direct numerical simulation (DNS) of swimmers in a binary (Newtonian) fluid mixture. In particular, we fully account for the deformable and penetrable nature of the interface between the two phase-separated fluids.

This chapter is organized as follows. First, we present the details of our theoretical model and numerical method. We then provide a comprehensive analysis of our DNS results, in which we observe two distinct motions at the interface, depending on the type of swimmer and the incidence angle: (1) transmission across the interface and (2) bouncing back from the interface. Finally, we also present a detailed analysis and characterization of the resulting steady-state behaviour.

2.2 Simulation Methods

2.2.1 The squirmer model

To model microswimmers, the squirmer model is employed in this chapter. It is a widely used model for a self-propelled particle in which the swimmer is represented as a spherical particle of radius a, with a modified stick boundary condition at its surface

[32, 50]. The surface velocity at a point $\boldsymbol{r}$ at the surface of the sphere is

$$\boldsymbol{u}^s(\vartheta) = \sum_{n=1}^{\infty} \frac{2}{n(n+1)} B_n P_n'(\cos\vartheta)\sin\vartheta\hat{\boldsymbol{\vartheta}}, \tag{2.1}$$

where $\vartheta = \cos^{-1}(\hat{\boldsymbol{r}} \cdot \hat{\boldsymbol{e}})$ is the polar angle between $\hat{\boldsymbol{r}}/|\boldsymbol{r}|$ the unit radial direction and $\hat{\boldsymbol{e}}$ the swimming direction, with $\hat{\boldsymbol{\vartheta}} = \hat{\boldsymbol{r}} \times (\hat{\boldsymbol{r}} \times \hat{\boldsymbol{e}})/\sin\vartheta$ the corresponding unit tangential vector. P_n' is the derivative of the Legendre polynomial of the nth order, and B_n is the magnitude of the nth mode. Here, this surface velocity has only tangential polar components, responsible for the self-propulsion of the swimmer, and the radial and azimuthal contributions to this have been neglected [34, 35].

In this chapter, only the first two modes in Eq. (2.1) are retained:

$$\boldsymbol{u}^s(\vartheta) = \left(B_1 \sin\vartheta + \frac{B_2}{2}\sin 2\vartheta\right)\hat{\boldsymbol{\vartheta}} \tag{2.2}$$

The first term in Eq. (2.2) represents the swimmer's source dipole, and coefficient B_1 is physically related to the steady-state swimming velocity of the squirmer via $U_0 = 2/3B_1$. The second term corresponds to the force dipole and is proportional to the swimmer's stresslet. The ratio $\beta = B_2/B_1$ determines the squirmer's swimming type and its *strength*. When β is negative, the squirmer is a pusher and generates extensile flow fields in the direction of propulsion; when β is positive, the squirmer is a puller generating contractile flow fields. The marginal case of $\beta = 0$ corresponds to a neutral particle that swims with the potential flow in the surrounding fluid. In what follows, we will refer to the microswimmer with $|\beta| \leqslant 1$ as being weak whereas $|\beta| \geqslant 4$ as being strong. Different types of squirmers can be mapped to different kinds of microorganisms in nature.

2.2.2   Smoothed profile method

To simulate the dynamics of a swimming system with fully resolved hydrodynamic interactions, we employ the smoothed profile (SP) method [36]. In this method, all boundaries, including both fluid/solid and fluid/fluid boundaries, are considered to possess a finite interfacial thickness ξ. This greatly simplifies the modeling and improves the computational efficiency of the method, as it avoids the need for complicated discretizations around the particles and the accompanying re-meshing of other DNS approaches, such as spectral/hp element methods [37]. Fluid/solid boundaries are implicitly accounted for by introducing a phase field function $\phi(\boldsymbol{r})$, which is equal to 1 within solid domains (inside the squirmer particles), is equal to 0 within the fluid domain (outside of the squirmer particles), and smoothly varies between 0 and 1 across the interface. Thus, such an interface can be represented by the gradient of the phase field, which will be nonzero only within the interfacial domains.

A modified (incompressible) Navier–Stokes equation is employed as the governing equation for the total fluid velocity $\boldsymbol{u}$:

$$\rho(\partial_t + \boldsymbol{u} \cdot \boldsymbol{\nabla})\boldsymbol{u} = \boldsymbol{\nabla} \cdot \boldsymbol{\sigma} + \rho(\phi \boldsymbol{f}_p + \phi \boldsymbol{f}_{sq}), \tag{2.3}$$

$$\boldsymbol{\nabla} \cdot \boldsymbol{u} = 0, \tag{2.4}$$

where $\boldsymbol{\sigma} = -p\mathbf{I} + \eta(\boldsymbol{\nabla}\boldsymbol{u} + \boldsymbol{\nabla}\boldsymbol{u}^{\mathrm{T}})$ is the Newtonian stress tensor (viscosity η) and ρ is the fluid density. The term $\phi \boldsymbol{f}_p$ appearing on the right-hand side of Eq. (2.3) is introduced to enforce the rigidity of the particles; likewise, the term $\phi \boldsymbol{f}_{sq}$ is introduced to enforce the "squirming" boundary condition at the surfaces of the particles [Eq. (2.2)].

The total velocity is defined in terms of the fluid velocity field $\boldsymbol{u}_f$ and the particle velocity field $\boldsymbol{u}_p$ as

$$\boldsymbol{u} = (1 - \phi)\boldsymbol{u}_f + \phi\boldsymbol{u}_p, \tag{2.5}$$

$$\phi\boldsymbol{u}_p = \sum_i \phi_i[\boldsymbol{V}_i + \boldsymbol{\Omega}_i \times \boldsymbol{R}_i], \tag{2.6}$$

where the first term $(1 - \phi)\boldsymbol{u}_f$ represents the velocity field of the binary fluid, whereas the second term $\phi\boldsymbol{u}_p$ represents the particles' velocity field, which is defined in terms of the positions $\boldsymbol{R}_i$, velocities $\boldsymbol{V}_i$, and angular velocities $\boldsymbol{\Omega}_i$ of the particles (where i is the particle index).

The dynamics of the rigid particles are determined by the Newton-Euler equations of motion,

$$\dot{\boldsymbol{R}}_i = \boldsymbol{V}_i, \tag{2.7}$$

$$\dot{\boldsymbol{Q}}_i = \mathrm{skew}(\boldsymbol{\Omega}_i) \cdot \boldsymbol{Q}_i, \tag{2.8}$$

$$M_i\dot{\boldsymbol{V}}_i = \boldsymbol{F}_i^H + \boldsymbol{F}_i^C + \boldsymbol{F}_i^{ext}, \tag{2.9}$$

$$\dot{\boldsymbol{J}}_i = \boldsymbol{N}_i^H + \boldsymbol{N}_i^{ext}, \tag{2.10}$$

where M_i is the mass of particle i, $\boldsymbol{J}_i = \boldsymbol{I}_i \cdot \boldsymbol{\Omega}_i$ is its angular momentum ($\boldsymbol{I}_i$ is the moment of inertia), $\boldsymbol{Q}_i$ is the orientation matrix, and $\mathrm{skew}(\boldsymbol{\Omega}_i)$ is the skew-symmetric angular velocity matrix. The hydrodynamic forces and torques are given by $\boldsymbol{F}_i^H$ and $\boldsymbol{N}_i^H$, $\boldsymbol{F}_i^C$ represents direct particle-particle interactions ($\boldsymbol{N}_i^C = 0$), and $\boldsymbol{F}_i^{ext}$ and $\boldsymbol{N}_i^{ext}$ are the external forces and torques, respectively.

The accuracy of the SP method has been extensively studied in previous works [36, 38–41]. For example, the friction and mobility tensors of nonspherical particle assemblies obtained from simulations at low Reynolds number (Re) are within $\lesssim 5\%$ of experimental values and high-precision solutions of the Stokes equation [40]. A similar degree of accuracy is found for the angular velocities of spherical particles under shear flow,
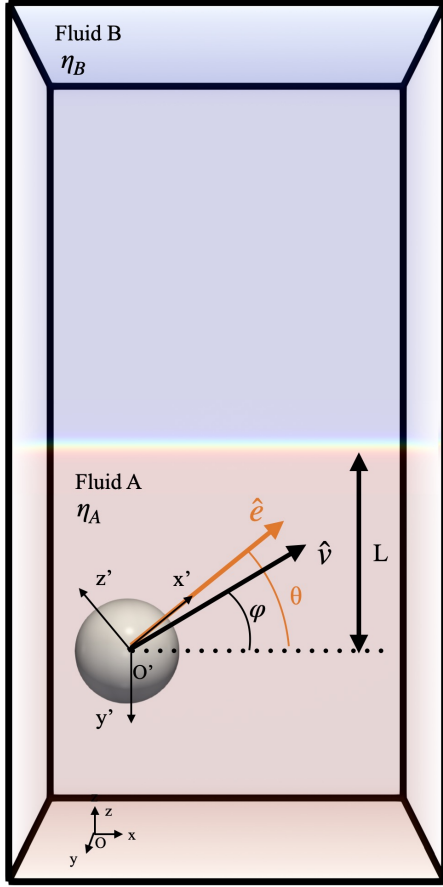
Figure 2.1. Schematic of a single swimmer near a planar interface normal to $\hat{\boldsymbol{z}}$. The swimmer's squirming axis is $\hat{\boldsymbol{e}}$, and its angle with the interface defines the orientation of the particle, which is denoted as θ. The direction of motion is given by $\hat{\boldsymbol{v}}$ with a relative angle to the interface φ.

for Re $\lesssim 10$ [42], and the ζ potential of charged colloidal dispersions [43]. Likewise, simulation results for the terminal velocity of a rising droplet in a binary fluid (density ratio $\rho_A/\rho_B \leq 1$) were within $\lesssim 8\%$ of the theoretical predictions [41]. Finally, we note that these benchmark simulations were performed using relatively coarse resolutions, for particles of size $a = 4 \sim 5\Delta$ with interfacial thickness $\xi = 2\Delta$ (Δ is the grid spacing).

2.2.3 Binary fluid model

The host fluid in our system is modelled as a phase-separating binary fluid mixture using the Cahn-Hilliard (CH) model, which, coupled with the Navier-Stokes hydrodynamics, yields the so-called model H [44, 45]. We refer to the two phases of this binary mixture

as fluids A and B. The spatial distributions of fluids A and B are given by order parameters $\psi_A(\mathbf{r})$ and $\psi_B(\boldsymbol{r})$, respectively, with $0 \leqslant \psi_\alpha \leqslant 1$. The composition of the fluid mixture is then determined by the order parameter $\psi(\boldsymbol{r})$,

$$\psi = \psi_A - \psi_B, \tag{2.11}$$

which takes a value of 1 in the A domain and a value of -1 in the B domain where the fractions of the constituent components (fluid and particles) must sum to unity,

$$\psi_A + \psi_B + \phi = 1. \tag{2.12}$$

To account for the binary fluid nature of the host fluid, an additional force term is introduced in Eq. (2.3),

$$\rho(\partial_t + \boldsymbol{u} \cdot \boldsymbol{\nabla})\boldsymbol{u} = \quad \boldsymbol{\nabla} \cdot \sigma - \psi \boldsymbol{\nabla} \mu_\psi - \phi \boldsymbol{\nabla} \mu_\phi + \rho(\phi \boldsymbol{f}_p + \boldsymbol{f}_{sq}),$$

where $\mu_\psi = \delta F / \delta \psi$ and $\mu_\phi = \delta F / \delta \phi$ are the locally defined chemical potentials with respect to ψ and ϕ, defined as functional derivatives of the Ginzburg-Landau free energy F. The time evolution of ψ is given by the following CH equation:

$$\frac{\partial \psi}{\partial t} + (\boldsymbol{u} \cdot \boldsymbol{\nabla})\psi = \kappa \nabla^2 \mu_\psi, \tag{2.13}$$

where κ is the mobility coefficient.

The free energy F can be represented as follows:

$$F = \int \mathrm{d}\boldsymbol{r} \left[f(\psi) + \frac{\alpha}{2}(\boldsymbol{\nabla}\psi)^2 + w\xi_p \psi (\boldsymbol{\nabla}\phi)^2 \right]. \tag{2.14}$$

In Eq. (2.14), the first term $f(\psi) = \frac{1}{4}\psi^4 - \frac{1}{2}\psi^2$ represents the Landau double-well potential and has two minima at $\psi = 1$ and -1. The second term is the potential energy associated with the fluid A/B interface. The third term represents the particles'

affinity for each of the fluid A/B phases. Thus, the chemical potentials are

$$\mu_\psi = f'(\psi) + \alpha\nabla^2\psi + w\xi_p(\boldsymbol{\nabla}\phi)^2, \tag{2.15}$$

and

$$\mu_\phi = 2w\xi_p(\boldsymbol{\nabla}\psi \cdot \boldsymbol{\nabla}\phi + \psi\nabla^2\phi). \tag{2.16}$$

In the present chapter, to keep the system as simple as possible, we assume that fluids A and B are immiscible but otherwise possess identical physical properties. In addition, we assume that the swimmers interact with the interface only hydrodynamically. Therefore, we set $w = 0$ in the present simulations.

2.3 Results

In this chapter, to investigate the dynamics of swimmers in complex fluids systems, we focus on the dynamics of a single particle near a fluid-fluid interface. All simulations are conducted for an immiscible A/B fluid system in a rectangular computational domain with dimensions of $32\Delta \times 32\Delta \times 64\Delta$ with Δ being the grid spacing and unit of length. Periodic boundary conditions are established in all directions. Fluids A and B share all the same physical properties, such as density and viscosity, and are initially phase separated in the z direction (see Fig. 2.1).

The radius of the squirmer is $a = 4\Delta$. The fluid-fluid interface thickness ξ_f is of order unity with the present choice of $\alpha = 1$ in Eq. (2.14), and the particle-fluid interface thickness ξ_p is set to 2. The parameter B_1 in Eq. (2.2) is set to 0.015, corresponding to a single-particle steady-state velocity of $U_0 = 2/3B_1 = 0.01$. The mobility κ [Eq. (2.13)], the shear viscosity η, and the mass densities $\rho = \rho_A = \rho_B = \rho_p$ are all set to 1. Then, the particle Re is Re $= \rho U_0 a/\eta = 0.08$, the Péclet number (Pe) is Pe $= U_0 a/\kappa = 0.08$, and the Schmidt number (Sc) is Sc $=$ Pe/Re $= 1$.

A schematic of our system is given in Fig. 2.1, which shows a single swimmer near a fluid-fluid interface. The deformable interfaces are initially planar and are located at $z = 0$ and $z = 32\Delta$. The distance between the center of mass of the swimmer and the nearest interface is denoted by L. We choose $L = 16\Delta$ as the initial condition, unless noted otherwise. In all simulations the initial separation is large enough that no appreciable interfacial deformations are observed during the transient regime, before the swimmer reaches its steady-state velocity. The orientation of an interface is given by the vector $\hat{z}$, $\hat{e}$ denotes the swimmer's polar axis which is taken to be parallel to the body frame $\hat{x}'$ axis, and $\hat{v} = V/|V|$ denotes the swimmer's direction of motion. Since the initial velocity of the particle along the y axis is set to 0, the swimmer will move only on the x-z plane. The orientation $\theta = \arcsin(\hat{z} \cdot \hat{e})$ is defined as the angle between the polar axis and the interface, whereas the angle for the direction of motion is defined by $\varphi = \arcsin(\hat{z} \cdot \hat{v})$.

2.3.1 Motion near the interface

To examine the motions of microswimmers near an interface, we conduct a series of simulations in which a swimmer approaches the interface with different angles of approach $\theta_{\mathrm{in}} \in (0, \pi/2)$. As motions with the same initial angle magnitude $|\theta_{\mathrm{in}}|$ are equivalent under a reflection symmetry we will focus on the case where $\theta_{\mathrm{in}} > 0$. After the swimmer leaves the interface, the outgoing angle is denoted by θ_{out}.

To understand the trajectories realised in our work consider a swimmer that starts off in fluid A and approaches the interface. Three distinct "collision" modes are observed once the swimmer reaches the interface, namely, (i) "bouncing," (ii) "sliding," and (iii) "penetrating" motions as illustrated in Fig. 2.2(a). In case (i), the swimmer bounces back into fluid A, avoiding fluid B, after performing a significant rotation within the interfacial domain and leaving the interface with $\theta_{\mathrm{out}} < 0$. In case (ii), the swimmer becomes trapped at the interface, swimming on the x-y plane with $\theta_{\mathrm{out}} \simeq 0$. Finally,
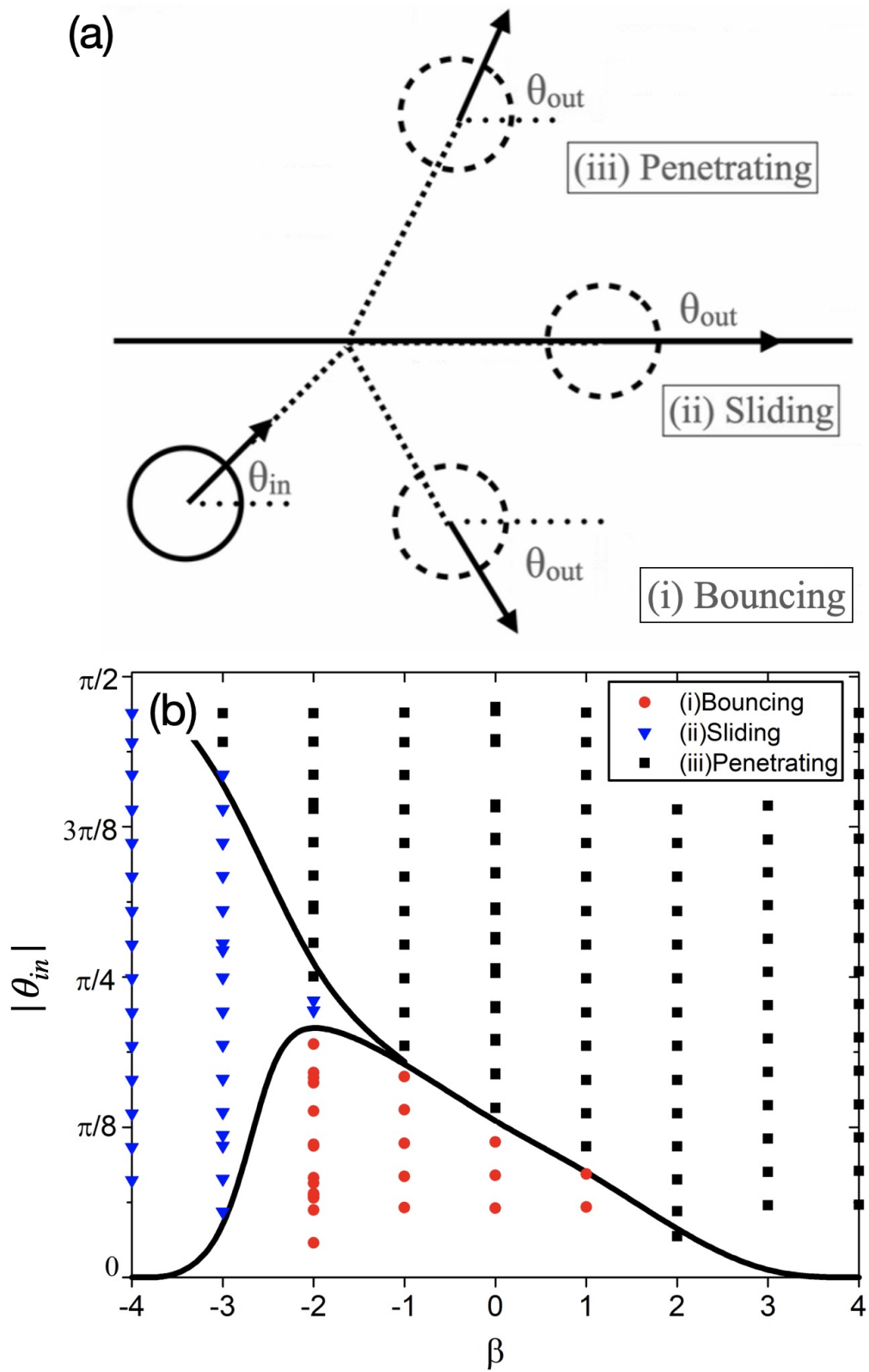
Figure 2.2. (a) Graphical illustration of the three different swimming modes for a swimmer after a single collision with the interface. (b) Diagram showing how these modes depend on the initial incidence angle $|\theta_{\mathrm{in}}|$ and swimming type β.
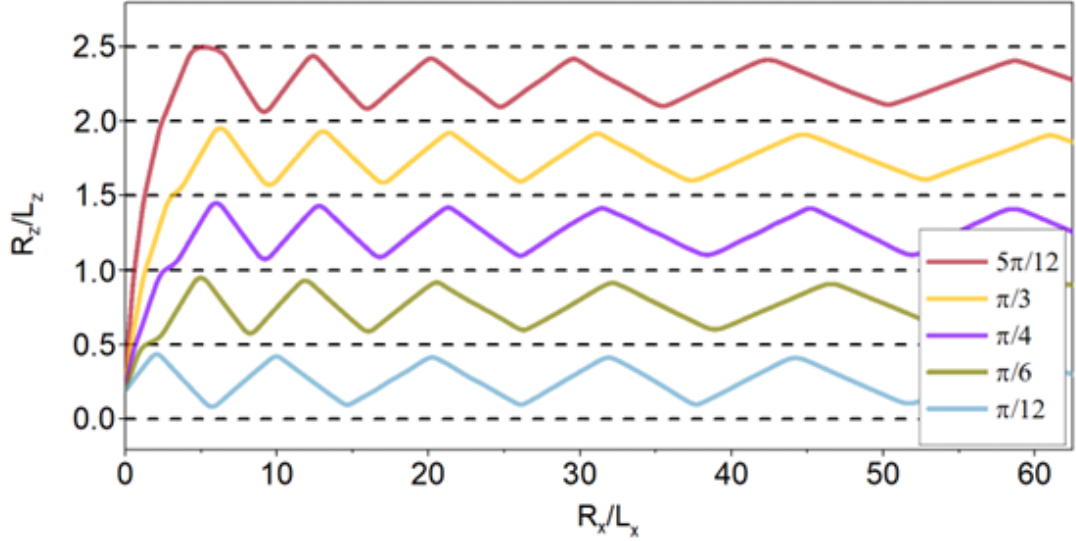
Figure 2.3. Swimmer ($\beta = -2$) trajectories showing repeated collisions with the interfaces (dashed lines) for various initial angles θ_{in}. The swimmer position is shown in units of the system height L_z and width L_x as it moves in z (vertical) and x (horizontal) respectively.

in case (iii), the swimmer passes through the interfacial barrier, swimming into fluid B with $\theta_{\text{out}} > 0$. See the movies in the supplemental material for animations of typical bouncing, sliding, and penetrating motion [60].

We conducted simulations with various initial angles θ_{in} and swimming parameters β to construct a phase diagram for the three types of motions (i)–(iii), as shown in Fig. 2.2(b). For weak swimmers, whereas the swimming strength and swimmer type play a role, the dominant factor determining the nature of the motion at the interface is the initial angle. Generally, if $|\theta_{\text{in}}|$ is small, the swimmer will bounce back from the interface (i). If $|\theta_{\text{in}}|$ is large, the swimmer will swim across the interface (iii). For strong swimmers, pushers prefer to slide on the interface with their swimming orientation aligned with the boundary (ii), whereas pullers are more inclined to cross the interface (iii).

We also performed long-time simulations to study repeated collisions with interfaces. The particle orientation is allowed to evolve under these repeated collisions. Due to the periodic boundaries, the approaching/departing process is repeated with the swimmer colliding with the interface at an incoming angle θ_{in} equal to the outgoing angle θ_{out}
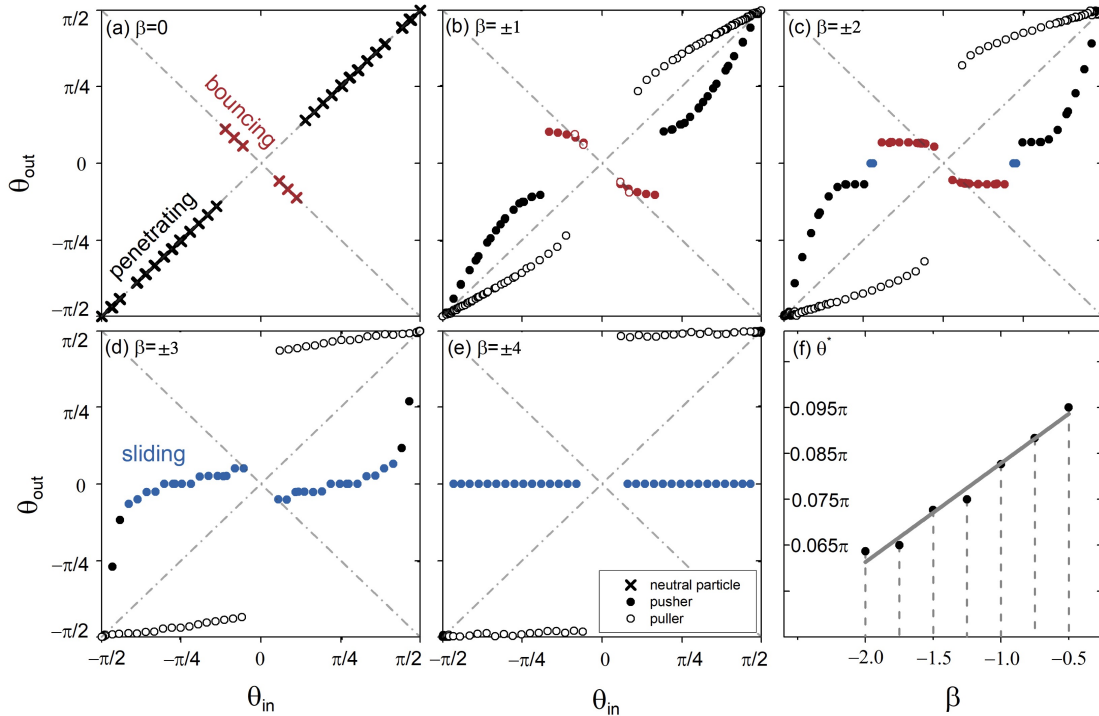
Figure 2.4. Changes in the orientation angle θ for swimmers with various β values: (a) $\beta = 0$; (b) $\beta = \pm 1$; (c) $\beta = \pm 2$; (d) $\beta = \pm 3$; (e) $\beta = \pm 4$. Filled circles represent pushers, whereas empty circles represent pullers. Black indicates the crossing motion, and red indicates the bouncing motion. Blue represents the special case in which the swimmer ultimately swims along the interface. (f) The final fixed angles θ^* as a function of pushers' swimming strength β.

of the previous collision. In the case of a pusher, a stable state of periodic back-and-forth motion between two interfaces is observed, as shown in Fig. 2.3. The steady-state motion is the same for all $\beta = -2$ pushers, regardless of the initial angle. For a puller, the magnitude of angle θ increases during each pass, and finally, the swimmer reaches a steady state moving perpendicular to the interface. Thus, we consider that the swimmer type has a strong effect on the dynamics near fluid-fluid interfaces.

2.3.2 Swimmer types

We consider the swimmer dynamics as a function of β. Based on our simulation results, we obtain a map f relating the initial angle $\theta_{\rm in}$ to the outgoing angle $\theta_{\rm out}$ as presented in Fig. 2.4. To interpret this diagram for the case of multiple encounters, the $\theta_{\rm out}$ achieved after one encounter should be read in as $\theta_{\rm in}$ for the subsequent encounter. The

24
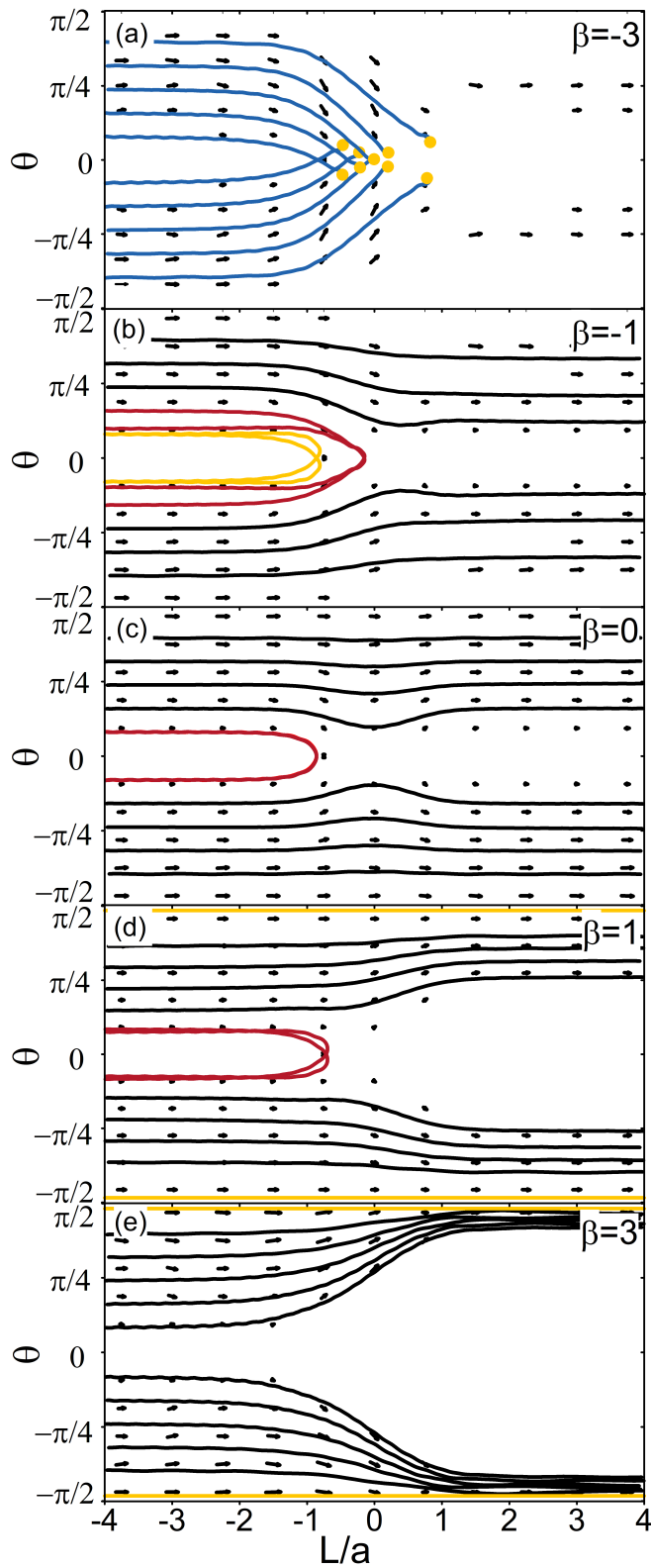
Figure 2.5. Quiver plot showing the time evolution of orientation angle θ for swimmers with various β values: (a) and (b) pushers with (a) $\beta = -3$, (b) $\beta = -1$; (c) neutral particle; (d) and (e) pullers with (d) $\beta = 1$, (e) $\beta = 3$. Black and red lines indicate crossing and bouncing-back motions, respectively, whereas blue lines are used for swimmers that end up in the sliding motion, swimming parallel to the interface. Yellow indicates the steady state for swimmers with non-zero β.

penetrating mode and the bouncing mode are represented in black and red, respectively. For a neutral particle, orientation angle θ shows no change after the swimmer leaves the interface, regardless of its motion (bouncing or penetrating), as illustrated in Fig. 2.4(a).

Figure 2.4(b)- 2.4(e) further illustrates the differences between pushers and pullers with the same $|\beta|$ values ($1 \leqslant |\beta| \leqslant 4$). Open symbols represent pullers, whereas filled symbols represent pushers. From these graphs, we can observe that the maps for swimmers with opposite values of β are nearly symmetric about the diagonal $\theta_{\text{out}} = \theta_{\text{in}}$, especially for the penetrating motion of weak swimmers (i.e., $\beta = \pm 1$). In other words, these maps are the inverse functions of each other. In general, swimmers with large initial angles, marked in black, swim across the interface. On the other hand, swimmers with small initial angles, marked in red, bounce back from the interface. However, the threshold angle that divides the bouncing and penetrating behaviors is different for different swimmers and depends on the β value. Even if pushers and pullers start from the same initial angle θ_{in} and exhibit the same swimming mode (penetrating or bouncing), their orientation angles will change in different ways. This is most easily seen from the penetrating trajectories of pullers and pushers, with the orientation angle increasing for the former ($\theta_{\text{out}} > \theta_{\text{in}}$) and decreasing for the latter ($\theta_{\text{out}} < \theta_{\text{in}}$). For pullers ($\beta > 0$), only two types of motion, penetrating and bouncing motion, are observed. For pushers ($\beta < 0$), an additional "sliding" state is observed for $\beta \leqslant -3$, marked in blue. The swimmers are trapped by the interface, swimming along it, even though their orientations are not completely aligned with the interface (i.e. θ_{out} is not necessarily zero).

Figure 2.5 shows how orientation angle θ changes as a function of the distance from the nearest interface. Taking $L = 0$ as the dividing point of penetrating motion, and $\theta = 0$ as the dividing point for bouncing motion, we can decompose a complete interaction with the interface into two parts, corresponding to the approaching and departing processes. We note that these two processes show a clear symmetry about the interface ($L = 0$) for the neutral swimmers (c) trajectories, which is not observed for pushers (a-b) or pullers

(i) Penetrating the interface perpendicular to the interface

(ii) Bouncing back and forth at a fixed angle θ*
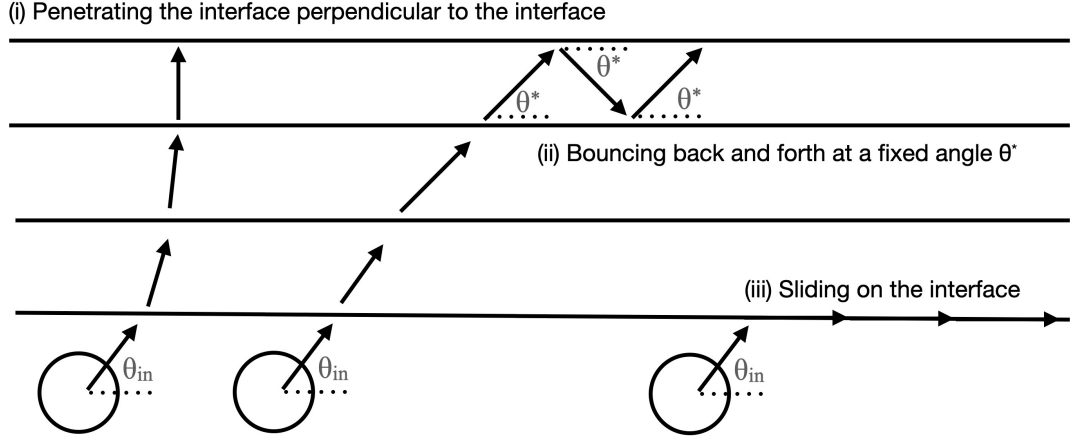
(iii) Sliding on the interface

Figure 2.6. Three types of stable states for swimmers: (i) A puller eventually swims perpendicular to the interface; (ii) a weak pusher eventually bounces back and forth between two interfaces with a certain angle whereas remaining in one of the fluid domains; (iii) a strong pusher eventually slides on the interface.

(d-e). Furthermore, for the case of pushers, the outgoing angle approaches a fixed value with the swimmers reaching a steady state in which they bounce back and forth periodically at this particular angle $\theta_{\text{out}} = -\theta_{\text{in}} = \theta^*$ [marked in yellow in Fig. 2.5(b)].

We note that the swimming strength also contributes to the hydrodynamic interactions near the interface. In particular, the change in orientation after crossing the boundary will be more pronounced for stronger swimmers. Thus, strong pullers will more quickly reach the stable state in which they swim perpendicular to the interface. For pushers for which the outgoing angle decreases, this can give rise to a sliding motion. The corresponding trajectories are marked in blue in Fig. 2.5(a). In such a case, the pusher can move along the interface, with half of its body in fluid A and the other half in fluid B. This motion is reminiscent of the equatorial anchoring of Janus particles at an oil–water interface [61]. However, the former is due to the symmetry of the fluid system about the interface, whereas the latter is due to the symmetrical structure of the amphiphilic particles. Additionally, according to Fig. 2.2(b), the range of initial angles that can lead to this sliding motion increases as the swimming strength of the pusher increases.

We now consider the formation of different final stable states. Due to the symmetry

considered in this chapter, i.e., alternating fluid layers with identical properties for the two fluids, the swimmer trajectories show convergence after several interfacial interactions. We conduct a series of simulations in the bouncing regime for different initial orientations θ_0, allowing the swimmer to collide with the interface several times. The orientation angle changes after each collision, approaching a steady-state value. Three distinct states are observed (see Fig. 2.6): (i) swimming perpendicular to the interface, (ii) bouncing back and forth at a fixed angle $\theta^\star$, or (iii) sliding on the interface. Multiple collisions can be considered as multiple iterations of the mapping $f(\theta_{\text{in}} \to \theta_{\text{out}})$, which represents the change in angle after a single collision with an interface (Fig. 2.4). After the mth collision, the swimmer has an orientation θ_{out}^m, which will be the incidence angle for the next $(m+1)$ collision, such that $\theta_{\text{in}}^{m+1} = \theta_{\text{out}}^m$. Figure 2.7 shows the changes in the swimmer orientation ($\beta = \pm 1$) after a sequence of $m = 6$ consecutive collisions. According to Fig. 2.7(a), the terminal angle of a weak puller will eventually converge to either $\pi/2$ or $-\pi/2$, regardless of the initial angle, marked yellow in Figs. 2.5(d) and 2.5(e). That is, after it has repeated the process of approaching an interface several times, a puller will eventually swim (i) perpendicular to the interface as shown in Fig. 2.6. A movie showing these repeated collisions and the resulting perpendicular alignment is given in the supplemental material [60].

For initial angles other than the boundary cases of $\theta = \pm\pi/2$, the terminal angle for a pusher will eventually converge (after repeated interfacial collisions) to an intersection point θ^* that is located in the bouncing motion regime as shown in Fig. 2.7(b). That is, pushers will always stabilize to a state in which they (ii) bounce back and forth at a fixed angle θ^*, as shown in Fig. 2.6. A movie showing these repeated collisions and the resulting bouncing back motion is given in the supplemental material [60]. This fixed angle θ^* depends on the value of β, as illustrated in Fig. 2.4(f).

In addition, for sufficiently strong pushers, (iii) sliding on the interface is also a possible steady state, in which they are trapped at the interface without any displacement in the

z axis and swim along it without any rotation [marked as yellow points in Fig. 2.5(a)], as shown in Fig. 2.6. A movie showing this sliding motion is given in the supplemental material.

2.4 Discussion

To the best of our knowledge, previous numerical studies of swimmer dynamics at interfaces [57, 62] have usually considered only far-field hydrodynamics or nonpenetrable surfaces. In this chapter we have considered a physical model in which swimmers interact with a soft, deformable, and penetrable interface. As a result, novel dynamics can be predicted and analyzed, such as the penetrating mode. In this mode, the swimmers pass through the interface and swim into another fluid.

The work of Gidituri *et al.* is related to ours [63]. They investigate the reorientation dynamics of spherical microswimmers trapped at fluid-fluid interfaces. A sinusoidal dependence between the reorientation velocity Ω_F and angle θ is proposed based on their analytical arguments. Their simulation results are in agreement with this prediction, $\Omega(\beta) = \hat{\Omega}_F(\beta) \sin 2\theta$, where the prefactor $\hat{\Omega}_F(\beta)$ depends linearly on β. To reproduce their conclusions, we also analyze our simulation data when swimmers cross the interface. As shown in the Supplemental Material, we are able to reproduce the sinusoidal dependence between the reorientation velocity Ω_F and the orientation θ. In addition, we also reproduce the linear dependence of the prefactor Ω_F on β. As expected (due to pusher/puller duality) for swimmers with opposite β values, these prefactors Ω_F have the same magnitude (opposite sign). Compared to the results of Gidituri *et al.* [63], the value we obtain for the slope of this prefactor is slightly decreased, but shows good quantitative agreement (within error bars). This difference is reasonable, considering the fact that our particle is not fixed to the interface, the interface is deforming, we introduce a smooth profile to represent the particles, and we use a discretized spatial domain to numerically solve for the equations of motion.
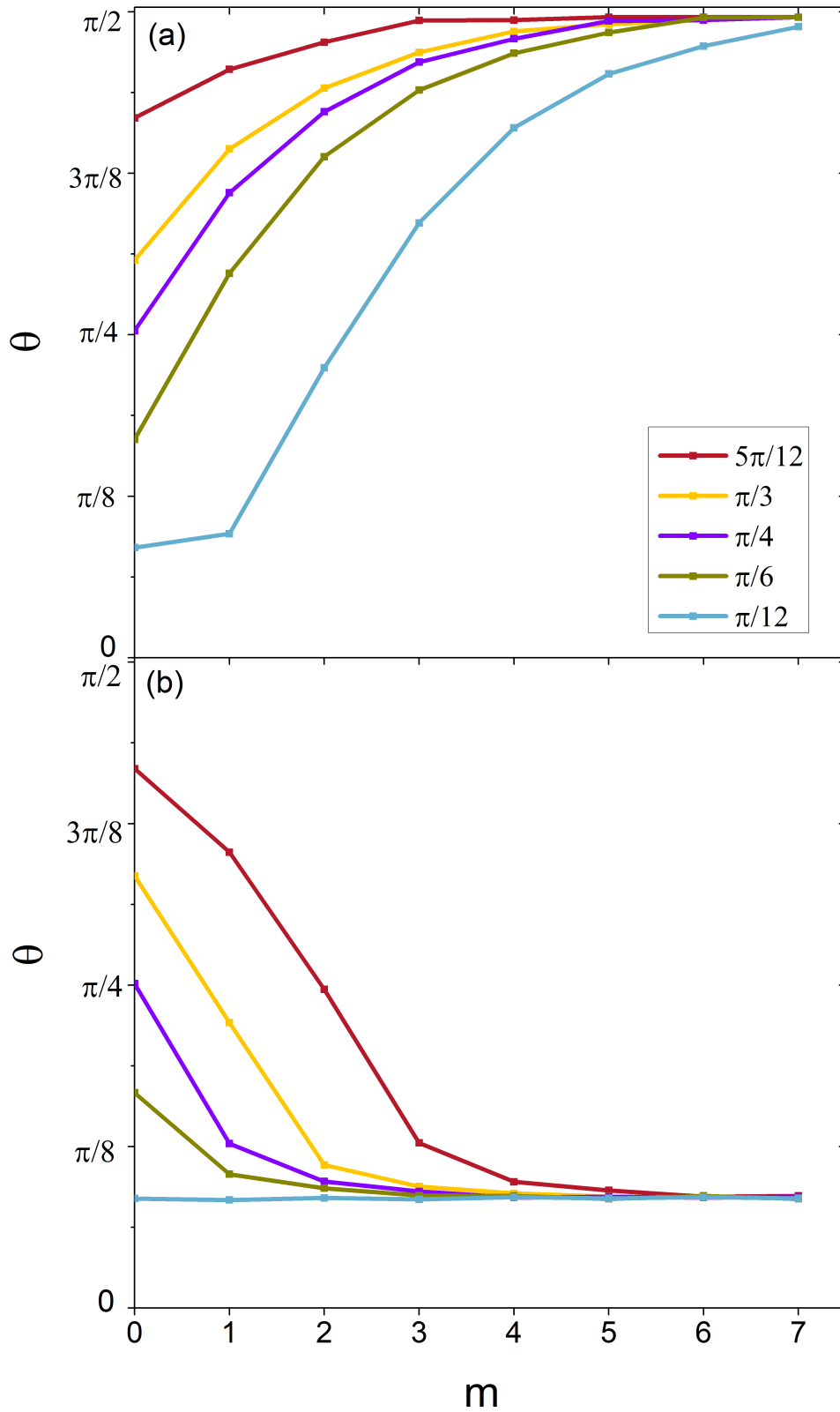
Figure 2.7. The changes in the orientation θ for (a) puller ($\beta = 1$); (b) pusher ($\beta = -1$) after it collides with the interface m times.

30

Although the literature for bacteria swimming near fluid interfaces is less developed, the mode in which the swimmer slides on the interface has previously been reported by Deng *et al.* [64], who observed that *Pseudomonas aeruginosa* adsorbed onto an oil-water interface. This sliding motion was also studied by means of a general multipole-expansion-based singularity model for swimming microorganisms [65]. Both pushers and pullers were predicted to accumulate at an oil-water interface, giving rise to large density inhomogeneities in many-particle systems. Highly organized movements with remarkable large-scale patterns (i.e., networks, complex vortices, or swarms), which result from the collective dynamics of microswimmers, are observed [4, 66]. In the present work we analyze only a single swimmer. This might help to explain why we predict instead that only strong pushers can be trapped by an interface. The work of Li and Ardekani [54] is probably the closest to ours, although they studied the motion of microswimmers near a solid wall. They found that a swimmer that was initially oriented toward the wall can escape (bounce back) if the strength of its squirming is sufficiently weak. However, they also reported another swimming mode in which very strong swimmers ($|\beta| > 7$) were observed to repeatedly bounce at the wall, which we do not observe in our simulations of a soft interface, although a hard/non-penetrable interface is, of course, accessible within our methodology.

2.5   Conclusions

In this chapter we analyze the dynamics of microswimmers in a binary fluid system. Our simulations are based on the SP method and the squirmer model. This allows accurate and efficient analysis of the dynamics near deformable fluid-fluid interfaces. Three qualitatively distinct dynamical modes emerge for swimmers approaching an interface, (i) penetrating, (ii) sliding, and (iii) bouncing. The dynamical properties depend on the swimmer type, the swimming strength, and the initial angle of approach. For a puller, the orientation angle is predicted to increase after the swimmer interacts

with the interface. This will eventually reach $\pm\pi/2$ after repeated interfacial collisions, after which the puller will swim perpendicular to the interface. For a pusher the orientation angle instead approaches a fixed oblique angle $\theta^\star$, which can be increasing or decreasing, depending on whether the initial orientation was smaller or greater than this angle, respectively. As a consequence of this, we observe that most pushers will eventually exhibit a steady-state mode in which they bounce between two interfaces along trajectories inclined at angle θ^*. This steady-state angle θ^* is related to the swimmer type. For the case of a strong pusher, swimming parallel to the interface emerges as another possible dynamical mode.

Our results provide a detailed analysis of the hydrodynamic interactions of microswimmers with a deformable fluid-fluid interface. This improves our understanding of microswimmer motion in environments involving soft interfaces, having some similarities with those found in biology. Our work may also have some relevance in the context of bioengineering applications. For example, we could also incorporate additional features into our model, such as nutrient chemotaxis. This represents an interesting aspect to be examined in future investigations.

2.6   Appendix

2.6.1   Inertial effects

All the simulations discussed above were conducted for a fixed Re (relative swimmer speed normalized with a momentum transport rate), a fixed Pe (relative swimmer speed normalized with a Ψ transport rate), and a fixed Sc (relative momentum transport rate normalized with a ψ transport rate), which are set to Re $= 0.08$, Pe $= 0.08$, and Sc $= 1$, respectively, meaning that inertial effects are expected to be negligible. To examine the contribution of inertial effects to the swimmer dynamics, we also conducted some additional simulations for different values of Re and Pe. Figure 2.8 shows the variation
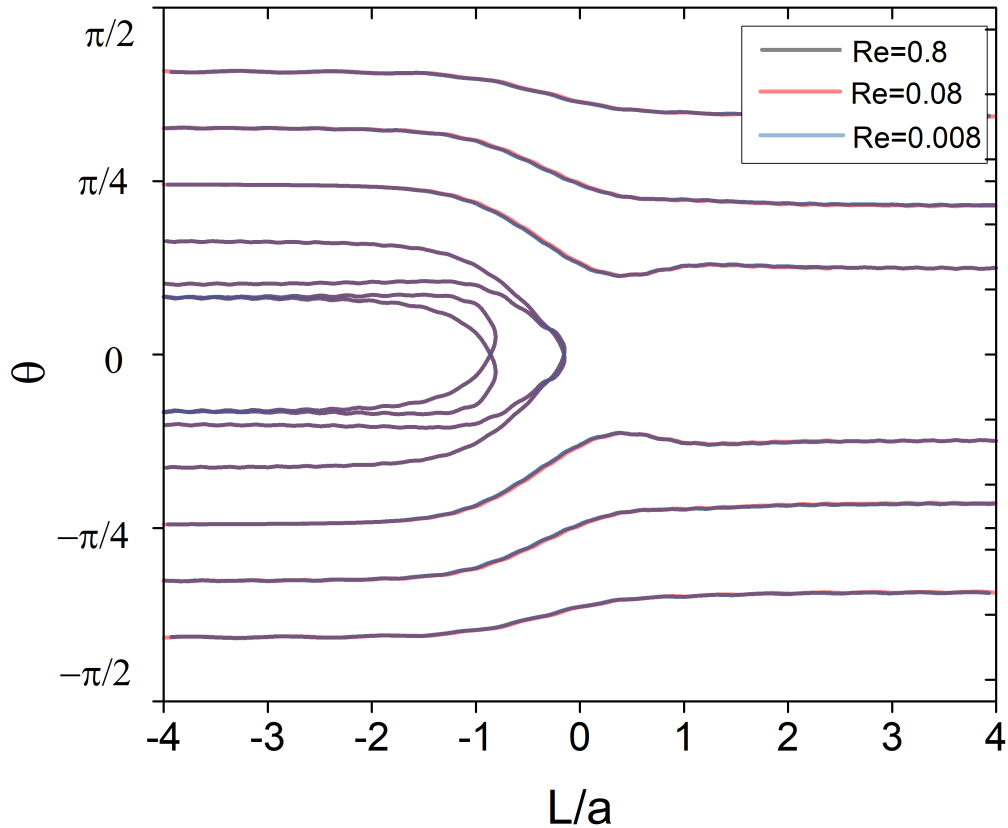
Figure 2.8. Variation in orientation angle θ with different Res. Black lines, red lines, and blue lines are used for the cases with Re $= 0.8$, 0.08, and 0.008, respectively.

in the orientation angle with the distance of the swimmer from the interface. The parameters used are the same as those in Fig. 2.5(f), except for the values of U_0. We compare three cases of pushers with Re $=$ Pe $= 0.008$, 0.08, and 0.8 in Fig. 2.8 where it is seen that the three trajectories perfectly collapse on each other. This result indicates that the inertial effects are negligible in our present simulations. Although the effect of Sc is not considered in the present work, it is also likely to contribute to the swimmer's dynamics as it approaches the interface. The exact mechanisms for this will require further investigation.

2.6.2 Software

All simulations presented in this chapter were conducted using the open-source version of the KAPSEL DNS software. KAPSEL has been developed in our laboratory to simulate the dynamics of solid particles dispersed in complex fluids. Detailed descriptions of KAPSEL are available online [67].

2.7 Supplemental Information

2.7.1 Supplementary movies

See Supplemental Material at `https://link.aps.org/doi/10.1103/PhysRevResearch.4.043202` for the simulation movies.

Supplementary Movie 1

Movie of a puller-type swimmer with $\beta = 3$ at an orientation angle of $\theta = \pi/3$, where the swimmer penetrates through the fluid-fluid interface.

Supplementary Movie 2

Movie of a pusher-type swimmer with $\beta = -4$ at an orientation angle of $\theta = \pi/3$, where the swimmer slides on the fluid-fluid interface.

Supplementary Movie 3

Movie of a weak pusher-type swimmer with $\beta = -2$ at an orientation angle of $\theta = \pi/3$, where the swimmer bounces back from the fluid-fluid interface.

Supplementary Movie 4

Identical to Supplementary Movie 1 but from a longer-term simulation. The swimmer reaches a steady state in which it repeatedly penetrates through the fluid-fluid interface [see Fig. 2.7(a)].

Supplementary Movie 5

Identical to Supplementary Movie 3 but from a longer-term simulation. The swimmer reaches a steady state in which it repeatedly bounces back from two adjacent fluid-fluid interfaces [see Fig. 2.7(b)].

2.7.2   Comparison with Gidituri *et al.*'s results

The present work is closely related to the work of Gidituri *et al.*. [63], in which they investigate the reorientation dynamics of spherical microswimmers trapped at fluid-fluid interfaces. The models they have used are the same as ours, although the numerical methods are different (notably, they use the Lattice-Boltzmann method to solve for the hydrodynamics). Focusing on this simpler case of a particle trapped at the interface (removing the translational degrees of freedom), allows for some analytical arguments to be made. For viscosity-matched fluids (the case we are interested in), only the B_2 term will contribute to the reorientation of the squirmer at the interface (they also neglect the higher order modes, $B_{n \geqslant 3} = 0$). This contribution can be modelled as a force-dipole

$$\boldsymbol{f}_{\pm} = \pm\hat{\boldsymbol{f}_0}\delta(\boldsymbol{r} \mp a\hat{\boldsymbol{e}}) \tag{2.17}$$

where $\hat{\boldsymbol{e}}$ the swimming axis, δ the Dirac delta function, and $B_2 = f_0 a/2\pi\eta\boldsymbol{R}^2$. The torque due to the rotation of this force-dipole (in the Stokes limit, and assuming a flat

interface), is given by

$$\boldsymbol{T} = 4\pi\eta\boldsymbol{R}^2\hat{\boldsymbol{e}}\cdot\hat{\boldsymbol{n}}(\hat{\boldsymbol{n}}\times\hat{\boldsymbol{e}}) = 2\pi\eta\boldsymbol{R}^2\sin 2\theta\hat{\boldsymbol{\tau}} \qquad (2.18)$$

with $\hat{\boldsymbol{\tau}}$ a unit vector perpendicular to the plane spanned by $\boldsymbol{e}$ and the interface normal $\boldsymbol{n}$, and θ the angle between $\hat{\boldsymbol{e}}$ and $\hat{\boldsymbol{n}}$. Thus, this predicts an angular velocity of the form $\Omega_F \propto \sin 2\theta$. The simulation results presented by Gidituri $et\ al.$ are in agreement with this prediction, $\Omega(\beta) = \hat{\Omega}_F(\beta)\sin 2\theta$, where the pre-factor $\hat{\Omega}_F(\beta)$ depends linearly on β.

In our work, although we consider the full swimmer dynamics and the "collisions" with the deformable interface (our particles are not trapped at the interface), we can still expect good agreement with these predictions (for small deformations and low-Reynolds number). To check this, we have taken our simulation data for the torque and angular velocity of the swimmer as it crosses the interface. As shown in Fig. 2.9(a), we are able to reproduce the sinusoidal dependence between the reorientation velocity Ω_F and the orientation θ. While we obtain a good overall agreement, there is considerable scattering of our measured data points around the expected sinusoidal behaviour. There are several factors that contribute to this deviation. First, our system is not exactly the same as that of Gidituri $et\ al.$ Since we are investigating the particle-interface collision dynamics, our particles are allowed to translate relative to the interface, in turn giving rise to non-zero interfacial deformations. While these deformations are small, there is a clear correlation between their amplitude and the deviations in the angular velocity [see Fig. 2.9(c)]. Second, is the fact that the particle positions used to obtain this data do not correspond exactly to the position of the interface, just the position at the closest approach, due to the discrete time-integration method that has been employed. Third, is the use of the smoothed interface and the spatial discretization of the underlying equations of motion, which results in a variation in the resolution of the particle volume/surface as it moves across the numerical grid. In addition, we also reproduce the linear dependence of the prefactor Ω_F on β, as seen in Fig. 2.9(b).

36
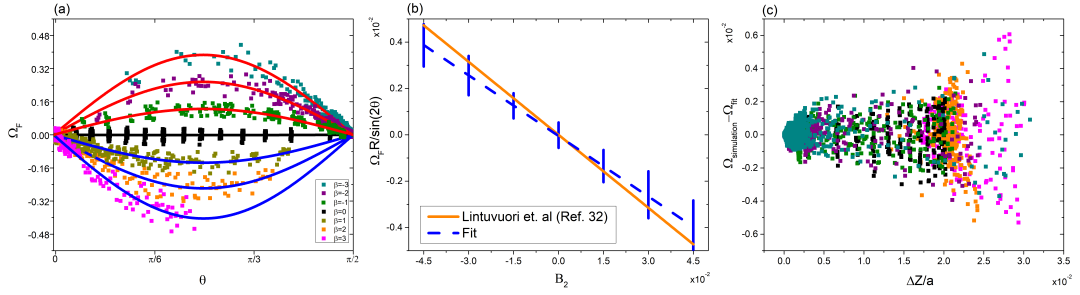
Figure 2.9. (a)The measured angular velocity Ω_F as a function of the orientation θ with various β values; (b)the coefficient $\Omega_F/\sin 2\theta$ as a function of the force dipole strength B_2. The error bars are estimated from the fluctuations around $\Omega_F - A_{\text{fit}}\sin(2\theta)$. (c) The error in the angular velocity $\Omega_{simulation} - \Omega_{fit}$ as a function of the displacement of the interface.

As expected (due to pusher/puller duality), for swimmers with opposite β values these prefactors Ω_F have the same magnitude (opposite sign). Compared to Gidituri's results, the value we obtain for the slope of this prefactor is slightly decreased, but shows good quantitative agreement (within error bars). We consider these differences to be reasonable, considering the previously mentioned differences in the setup and the approximations used by our numerical methods.

Chapter 3

Dynamics of microswimmers near a liquid-liquid interface with viscosity difference

3.1 Introduction

Across the natural world, it is common for microswimmers to navigate through complex fluid environments, e.g., spermatozoa in seminal plasma and cervical mucus [68–70]. Trans-membrane transport of bacteria and viruses is also a key stage in infection [71]. Therefore, research into the dynamics of swimmers in such environments is of vital importance to understand many biological transport processes, as well as for the development of potential future artificial micro-machines, which could be used for targeted delivery in complex fluid environments [48, 49, 72–74].

Most studies on the dynamics of microswimmers in complex multi-phase systems have focused on swimming in the vicinity of boundaries, mainly solid-fluid boundaries [53, 54, 56, 57, 75–79] and fluid-air interfaces [57, 80]. For example, Lauga *et al.* [78] observed

that *E. coli* was shown to exhibit a clockwise circular swimming motion near a solid-fluid boundary, whereas Leonardo *et al.* [80] reported a counterclockwise rotation near a free surface, such as the fluid-air interface. In both cases, this circular motion can be explained as arising from the hydrodynamic interactions.

However, few theoretical studies have attempted to construct a general hydrodynamic description of microswimmers near (complex) fluid-fluid interfaces [63, 81–83]. This may be due to the high computational costs associated with treating deformable and penetrable boundaries. Of particular (biological) importance is the case where fluids have mismatched viscosities. This can dramatically affect the swimmer dynamics. For example, spermatozoa exhibit very different tail waveforms, depending on the viscosity of the fluid [68, 84]. Sperm in low viscosity medium has a significant side-to-side movement across the directional axis. However, in high-viscosity fluids, e.g., mucus, such head yaw is reduced by using a distinct "meandering" waveform with less lateral movement across the directional axis. In this way, the spermatozoa are able to swim with approximately the same velocity in either fluid, saline or mucus, despite the large viscosity difference between the two.

Previously, we have studied the dynamics of microswimmers near a soft, deformable and penetrable interface in an isoviscous system[85]. In this chapter, we extend our work to consider the dynamics of swimmers near the interface of two fluids with mismatched viscosities. First, we review the computational model we have used, and detail how it is extended to take the variable viscosity into account. Then, we analyse the effect of the viscosity on the motion of the swimmer in the low Reynolds-number regime. As we previously found for the isoviscous case, different initial trajectories can lead to motions that we characterise as "bouncing", "sliding", and "penetrating". In addition to these modes, we also observe a new dynamical "hovering" mode, in which the swimmer tends to move parallel to the interface, at a fixed (non-zero) distance. By analysing the trajectories and time evolution of orientations, several symmetric pairs for bouncing or

penetrating motions are found which indicates the pushers/pullers duality. Compared to the isoviscous case, we find that a viscosity difference can significantly affect the dynamics during the collision with the interface, i.e., the relationship between incoming and outgoing angles. Finally, we provide an analysis of the dynamics of microswimmers in the hovering motion. Interestingly, both the trajectories and time evolution of angles, including their orientations and directions of motions, are highly similar to that of microswimmers near a solid wall.

3.2   Simulation Methods

3.2.1   The squirmer model

We model swimmers as spherical squirmers, one of the most widely employed mathematical models for microswimmers[32, 50]. Thus, swimmers are represented as rigid spherical particles, with a modified stick boundary condition at their surface. To simplify the description, we only consider the tangential components of the surface velocity, ignoring both azimuthal and radial contributions, which is the usual approximation[34, 35]. The surface velocity is given as

$$\boldsymbol{u}^s(\vartheta) = \sum_{n=1}^{\infty} \frac{2}{n(n+1)} B_n P'_n(\cos\vartheta) \sin\vartheta \hat{\boldsymbol{\vartheta}}, \tag{3.1}$$

where $\vartheta = \cos^{-1}(\hat{\boldsymbol{r}} \cdot \hat{\boldsymbol{e}})$ is the polar angle between the swimming direction $\hat{\boldsymbol{e}}$ and $\hat{\boldsymbol{r}}$, a unit vector directed from the centre of the squirmer toward the corresponding point on its surface and $\hat{\boldsymbol{\vartheta}}$ is the unit vector orthogonal to $\hat{\boldsymbol{r}}$. P'_n is the derivative of the Legendre polynomial of the nth order, and B_n is the magnitude of each mode.

Only the first two modes in Eq. (3.1) are retained,

$$\boldsymbol{u}^s(\vartheta) = B_1(\sin\vartheta + \frac{\beta}{2}\sin 2\vartheta)\hat{\boldsymbol{\vartheta}}, \tag{3.2}$$

The coefficient of the first term in Eq. (3.2), B_1, determines the steady-state swimming velocity of the squirmer $U_0 = 2/3B_1$. The coefficient of the second mode, B_2, determines the stress exerted by the particles on the fluid. The ratio $\beta = B_2/B_1$ determines the swimming type and strength. When β is negative, the squirmer is a pusher, which swims generating an extensile flow field (e.g., *E. coli*); when β is positive, the squirmer is a puller, which swims generating a contractile flow field (e.g., *C. reinhardtii*). The marginal case of $\beta = 0$ corresponds to a neutral particle, which is accompanied by a potential flow (e.g., *Volvox*). In what follows, we will refer to squirmers with $|\beta| \leqslant 1$ as being weak, and those with $|\beta| \geqslant 4$ as being strong.

3.2.2 Smoothed profile method for binary fluids

To simulate the dynamics of particles dispersed in an immiscible binary A/B fluid system, while fully accounting for the hydrodynamic interactions, we consider the coupled equations of motion for the solid particles and the component fluids within the model-H representation, i.e., the Newton-Euler and Cahn-Hilliard Navier-Stokes equations [44, 45]. Furthermore, to allow for efficient calculations of many-particle systems, while still providing an accurate description of the many-body hydrodynamic interactions, we employ the Smooth Profile (SP) method [36]. Within this approximation, sharp particle boundaries are replaced by diffuse interfaces of finite thickness. The solid particle domains are thus defined using a continuous order parameter or phase field ϕ over the whole computational domain. The A/B fluid phases are likewise defined in terms of the corresponding A/B order parameters ψ_A and ψ_B. This allows us to easily couple the rigid-body dynamics to the dynamics of the (phase-separating) fluids. In what follows we briefly describe how to solve for the (coupled) rigid-body dynamics, phase-separating dynamics, and fluid dynamics. Detailed descriptions of the SP method and its implementation can be found in our earlier publications.[36, 38–40]

3.2.2.1 Particle dynamics

The rigid particle dynamics are determined by Newton-Euler equations of motion:

$$\dot{\boldsymbol{R}}_i = \boldsymbol{V}_i, \tag{3.3}$$

$$\dot{\boldsymbol{Q}}_i = \mathrm{skew}(\boldsymbol{\Omega}_i) \cdot \boldsymbol{Q}_i, \tag{3.4}$$

$$M_i \dot{\boldsymbol{V}}_i = \boldsymbol{F}_i^H + \boldsymbol{F}_i^C + \boldsymbol{F}_i^{ext}, \tag{3.5}$$

$$\boldsymbol{I}_i \cdot \dot{\boldsymbol{\Omega}}_i = \boldsymbol{N}_i^H + \boldsymbol{N}_i^{ext}, \tag{3.6}$$

where $\boldsymbol{R}_i$, $\boldsymbol{Q}_i$, $\boldsymbol{V}_i$, $\boldsymbol{\Omega}_i$ are the positions, orientation matrices, velocities, and angular velocities of particle i, respectively. M_i is the masses, and $\boldsymbol{I}_i = 2/5 M_i a_i{}^2$ is moments of inertia for sphere particle i with radius a_i. $\mathrm{skew}(\boldsymbol{\Omega}_i)$ is the skew-symmetric matrix for the angular velocity. The hydrodynamic forces and torques are given by $\boldsymbol{F}_i^H$ and $\boldsymbol{N}_i^H$. $\boldsymbol{F}_i^C$ represents direct particle-particle interactions ($\boldsymbol{N}_i^C = 0$), and $\boldsymbol{F}_i^{ext}$ and $\boldsymbol{N}_i^{ext}$ are the external forces and torques, respectively.

Within the SP method, the particle domain is accounted for by an order parameter $\phi(\boldsymbol{r})$, which can be interpreted as the volume fraction of the solid component in the system

$$\phi(\boldsymbol{r}) = \sum_i \phi_i(\boldsymbol{r}), \tag{3.7}$$

where ϕ_i is the phase-field for particle i. This particle phase field is defined such that it is equal to 1 in the solid domain, 0 in the fluid domain, and smoothly interpolates between the two domains across the interfaces (of width ξ_p). In this way, the boundaries can be represented through the gradient of the phase field. We can then define the velocity field for the particle domain as

$$\boldsymbol{u}_p = \frac{1}{\phi} \sum_i \phi_i [\boldsymbol{V}_i + \boldsymbol{\Omega}_i \times \boldsymbol{R}_i]. \tag{3.8}$$

3.2.2.2 Phase-separating dynamics

The order parameters for the A and B phases, $\psi_A(\mathbf{r})$ and $\psi_B(\mathbf{r})$, represent the volume fractions of the constituent components ($0 \leqslant \psi_\alpha \leqslant 1$). Furthermore, since the sum total of the volume fraction of all components (fluids and particles) is constrained to be unity,

$$\psi_A + \psi_B + \phi = 1, \tag{3.9}$$

the composition of the A/B phase-separating fluid can be described in terms of a single order parameter $\psi(\mathbf{r})$,

$$\psi = \psi_A - \psi_B. \tag{3.10}$$

This order parameter $\psi(\mathbf{r})$ is defined to be is equal to 1 in the A domain and -1 in the B domain.

The dynamics for $\psi(\mathbf{r})$ is determined by the following modified Cahn-Hilliard equation,

$$\frac{\partial \psi}{\partial t} + (\mathbf{u} \cdot \boldsymbol{\nabla})\psi = \kappa \nabla^2 \mu_\psi, \tag{3.11}$$

where $\mathbf{u}$ is the total velocity field, κ is the mobility coefficient, and $\mu_\psi = \delta\mathcal{F}/\delta\psi$ is the chemical potential associated with the order parameter ψ. In what follows we will also need to account for the fluid-particle interactions using a second chemical potential associated with the ϕ order parameter, $\mu_\phi = \delta\mathcal{F}/\delta\phi$. These chemical potentials are derived from the Ginzburg-Landau free energy function,

$$\mathcal{F}[\psi, \phi] = \int \mathrm{d}\mathbf{r} \left[f(\psi) + \frac{\alpha}{2}(\boldsymbol{\nabla}\psi)^2 + w\xi_p \psi(\boldsymbol{\nabla}\phi)^2 \right] \tag{3.12}$$

The first term in the integrand of Eq. (3.12), $f(\psi) = \frac{1}{4}\psi^4 - \frac{1}{2}\psi^2$ represents the Landau double-well potential, with two minima at $\psi = 1$ and -1. The second term is the potential energy associated with the fluid A/B interface, the third term represents the particles' affinity for each of the fluid A/B phases. The chemical potentials corresponding

to this free-energy function are then

$$\mu_\psi = f'(\psi) + \alpha\nabla^2\psi + w\xi_p(\boldsymbol{\nabla}\phi)^2 \tag{3.13}$$

$$\mu_\phi = 2w\xi_p(\boldsymbol{\nabla}\psi \cdot \boldsymbol{\nabla}\phi + \psi\nabla^2\phi). \tag{3.14}$$

In what follows we assume that the particles will interact with the interface hydrodynamically but not chemically and so we set $w = 0$ in all simulations reported below.

3.2.2.3   Fluid dynamics

The total velocity, which accounts for both fluid and particle domains, is defined as

$$\boldsymbol{u} = (1 - \phi)\boldsymbol{u}_f + \phi\boldsymbol{u}_p, \tag{3.15}$$

where the first term gives the fluid velocity field and the second term the particle velocity field. Then, the time evolution of this total flow field $\boldsymbol{u}$ is given by a modified version of the Navier-Stokes and continuity equations,

$$\rho(\partial_t + \boldsymbol{u} \cdot \boldsymbol{\nabla})\boldsymbol{u} = \boldsymbol{\nabla} \cdot \boldsymbol{\sigma} + \rho(\phi\boldsymbol{f}_p + \boldsymbol{f}_{sq}) - \psi\boldsymbol{\nabla}\mu_\psi - \phi\boldsymbol{\nabla}\mu_\phi, \tag{3.16}$$

$$\boldsymbol{\nabla} \cdot \boldsymbol{u} = 0 \tag{3.17}$$

where $\boldsymbol{\sigma}$ is the Newtonian stress tensor, defined in terms of the total fluid velocity as

$$\boldsymbol{\sigma} = -p\mathsf{I} + \eta[\boldsymbol{\nabla}\boldsymbol{u} + (\boldsymbol{\nabla}\boldsymbol{u})^T] \tag{3.18}$$

where I is the unit tensor and η is the spatially varying viscosity. The term $\phi\boldsymbol{f}_p$ appearing on the right-hand side of Eq. (3.16) is the body force required to satisfy the rigidity constraint of the particles, the term $\phi\boldsymbol{f}_{sq}$ is the force needed to enforce the "squirming" boundary condition at their surface of the swimmers (Eq. (3.2)), and final two terms come from the binary-fluid nature of the host fluid.

In the present study, to keep the system as simple as possible, we assume that fluids A and B are strongly immiscible, but otherwise possess identical physical properties, except for their viscosities. Let η_A and η_B represent the viscosity of fluids A and B, respectively, and η_p the viscosity of the particle domains. The total phase-dependent viscosity $\eta(\boldsymbol{r})$ is defined as

$$\eta(\boldsymbol{r}) = \eta_A \psi_A(\boldsymbol{r}) + \eta_B \psi_B(\boldsymbol{r}) + \eta_p \phi(\boldsymbol{r}) \tag{3.19}$$
$$= \eta_A \left(\psi_A(\boldsymbol{r}) + \lambda \psi_B(\boldsymbol{r}) \right) + \eta_p \phi(\boldsymbol{r}),$$

where $\lambda = \eta_B/\eta_A$ is the fluid viscosity ratio.

3.3   Results

In this study, we conducted three-dimensional direct numerical simulations (DNS) of a single particle near an A/B fluid-fluid interface. In all cases, we use a rectangular simulation box of dimensions $(l_x, l_y, l_z) = (32\Delta, 32\Delta, 64\Delta)$, where Δ is the grid spacing and the unit of length. Periodic boundary conditions are established in all directions. The radius of the squirmer is set to $a = 4\Delta$. The parameter B_1 in Eq. (3.2) is set to 0.015, corresponding to a single-particle steady-state velocity of $U_0 = 2/3B_1 = 0.01$. The mobility κ (Eq. (3.11)), and the mass densities for both fluids and particles $\rho = \rho_A = \rho_B = \rho_p$ are all set to 1. We set the viscosity of the particle and fluid A to be equal to unity, $\eta_p = \eta_A = 1$, and vary the viscosity of fluid B in the range $1/10 \leqslant \eta_B \leqslant 10$. Then the particle Reynolds number $Re = \rho U_0 a/\eta$ is 0.08 in fluid A, while in fluid B it is from 0.008 to 0.8. The fluid-fluid interface thickness ξ_f is of order unity with the present choice of parameter $\alpha = 1$ in Eq. (3.12), and the particle–fluid interface thickness ξ_p is set to 2.

A schematic representation of our system is given in Fig. 3.1, which shows a single swimmer near a fluid-fluid interface. The system is initialized to be phase separated
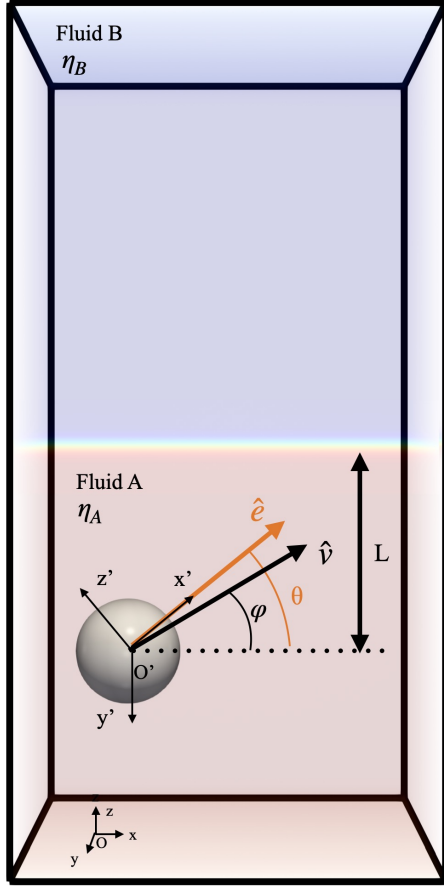
Figure 3.1. Schematic representation of a single swimmer near an A/B fluid-fluid interface normal to $\hat{\boldsymbol{z}}$. The angles θ and φ are here the angles between the squirming axis and the interface, and the direction of motion and the interface, respectively.

along the z direction. The swimmer is initially located in Fluid A (the host fluid). The distance between the centre of mass of the swimmer and the interface is L, with $L_{t=0} = -16\Delta$ unless noted otherwise. This initial distance from the interface is large enough to allow the particle to attain its steady-state velocity before any appreciable particle/interface interactions are observed. The orientation of the interface is specified by its normal vector, $\hat{\boldsymbol{z}}$, that of the swimmer's motion by its normalized velocity vector $\hat{\boldsymbol{v}} = \boldsymbol{V}/|\boldsymbol{V}|$, which need not correspond to its squirming axis $\hat{\boldsymbol{e}}$. The initial orientation of the particle is fixed to lie in the x-z plane, which will constrain its motion to this plane (i.e., $V_y = 0$). The x component of the position is R_x. The orientation angle $\theta = \arcsin\left(\hat{\boldsymbol{z}} \cdot \hat{\boldsymbol{e}}\right)$ is defined as the angle between the squirming axis and the interface, while the direction of motion is defined by $\varphi = \arcsin\left(\hat{\boldsymbol{z}} \cdot \hat{\boldsymbol{v}}\right)$.
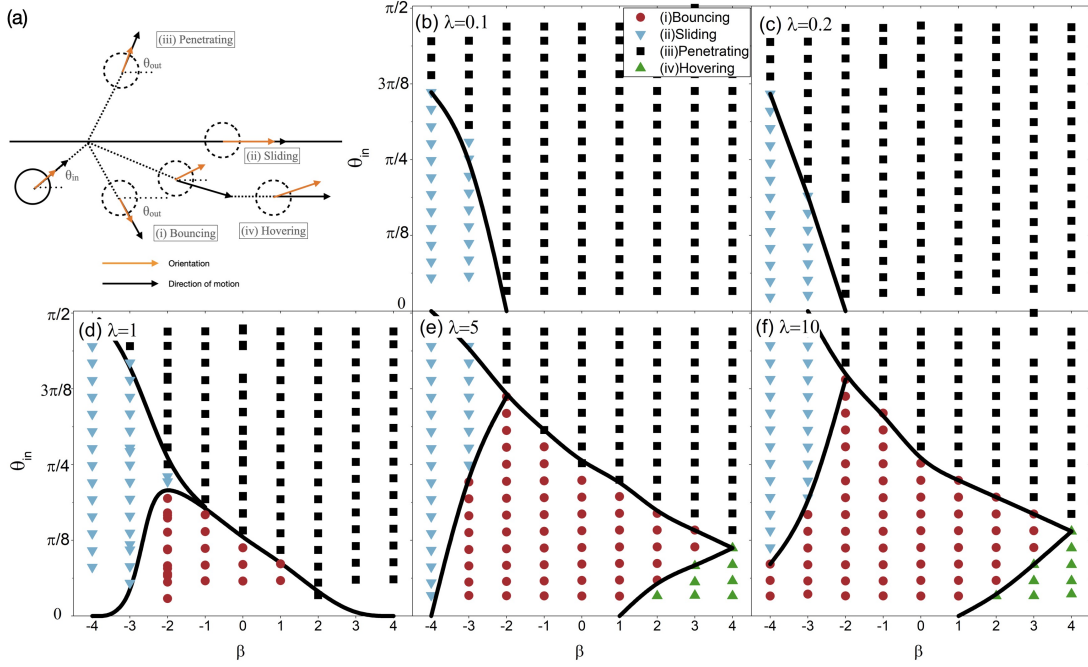
Figure 3.2. (a) Graphical illustration of the four collision modes of a swimmer with an interface. Black arrows indicate the swimmer's direction of motion, yellow arrows the swimmer's orientation; (b)–(f) Diagram showing how these modes depend on the initial incidence angle θ_{in} and swimmer type β for various viscosity ratios (b) $\lambda = 0.1$, (c) $\lambda = 0.2$, (d) $\lambda = 1$, (e) $\lambda = 5$, and (f) $\lambda = 10$.

To understand the dynamics of a swimmer near an interface for fluids with mismatched viscosities, we conduct a series of simulations in which the swimmer is initially in host fluid A, approaches the interface at an incoming angle θ_{in}, and exits this "collision" with an outgoing angle θ_{out}. Given the geometry of our setup, we can focus only on collisions with $\theta_{\text{in}} > 0$ (i.e., the swimmer collides with the lower interface), as those for $\theta_{\text{in}} < 0$ are equivalent due to the reflection symmetry. We consider various initial angles θ_{in} and swimming parameters β, together with a variety of different viscosity ratios $\lambda = 0.1, 0.2, 1, 5,$ and 10, in order to construct a phase diagram for the four distinct dynamical modes that result: (i) "penetrating", (ii) "sliding", (iii) "bouncing" and (iv) "hovering", as illustrated in Fig. 3.2(a). The first three of these modes are also observed in the case of isoviscous fluids ($\lambda = 1$), as reported in our previous work[85]. In case (i), the swimmer approaches the interface and exhibits a significant rotation within the interfacial domain, bouncing back into the host fluid A and avoiding fluid B, leaving the interface with $\theta_{\text{out}} < 0$. In case (ii), the swimmer becomes trapped at the

interface, swimming in the x-y plane with $\theta_{\text{out}} = 0$. In case (iii), the swimmer crosses the interfacial region separating the fluids, swimming into fluid B with $\theta_{\text{out}} > 0$. In case (iv), which is only observed for $\lambda \neq 0$, the swimmer direction of motion shows characteristic oscillations as it approaches and turns away from the interface, before eventually swimming parallel to the interface ($\theta_{\text{out}} = 0$) at a fixed distance greater than the particle radius $|L| > a$. Unlike for the bouncing motion, where the swimmer is able to reorient and swim away from the interface with $\theta < 0$, in the hovering motion the swimmer exhibits a partial reorientation to smaller angles, but it is always pointing towards the interface $\theta > 0$. At the steady state, the self-propulsion will balance with the hydrodynamic interactions with the interface, allowing the swimmer to propel itself parallel to the interface, even though the orientation of the swimmer is not aligned with the interface. Our results are summarized in the phase diagram of Fig. 3.2(b)–(f).

In our previous work on isoviscous systems, we have investigated how the collision dynamics depend on the angle of approach θ_{in} and the swimming mode β. For weak swimmers, we observed either penetrating or bouncing motion, depending on the initial orientation: penetration (bouncing) for large (small) angle magnitudes. The bouncing motion is more prevalent for pushers ($\beta < 0$) than pullers ($\beta > 0$), with the latter able to penetrate the interface at smaller angles. Strong pushers usually slide on the interface. The main role of the swimming mode β is to shift the boundary between penetrating and bouncing domains. These results are summarized in Fig. 3.2(d).

In the case of mismatched viscosities, the focus of the current work, we found that the viscosity ratio λ has a significant effect on the swimmer's motion, as can be seen in Fig. 3.2. For viscosity ratios less than unity $\lambda < 1$, corresponding to swimmers starting in the high viscosity fluid, the bouncing mode is never observed, rather the penetrating mode dominates for all but the strongest pushers. For such strong pushers, the sliding state can also be observed at small to moderate incoming angles. Figure 3.2(b) and (c) show the results for $\lambda = 0.1$ and 0.2. For viscosity ratios larger than unity $\lambda > 1$,
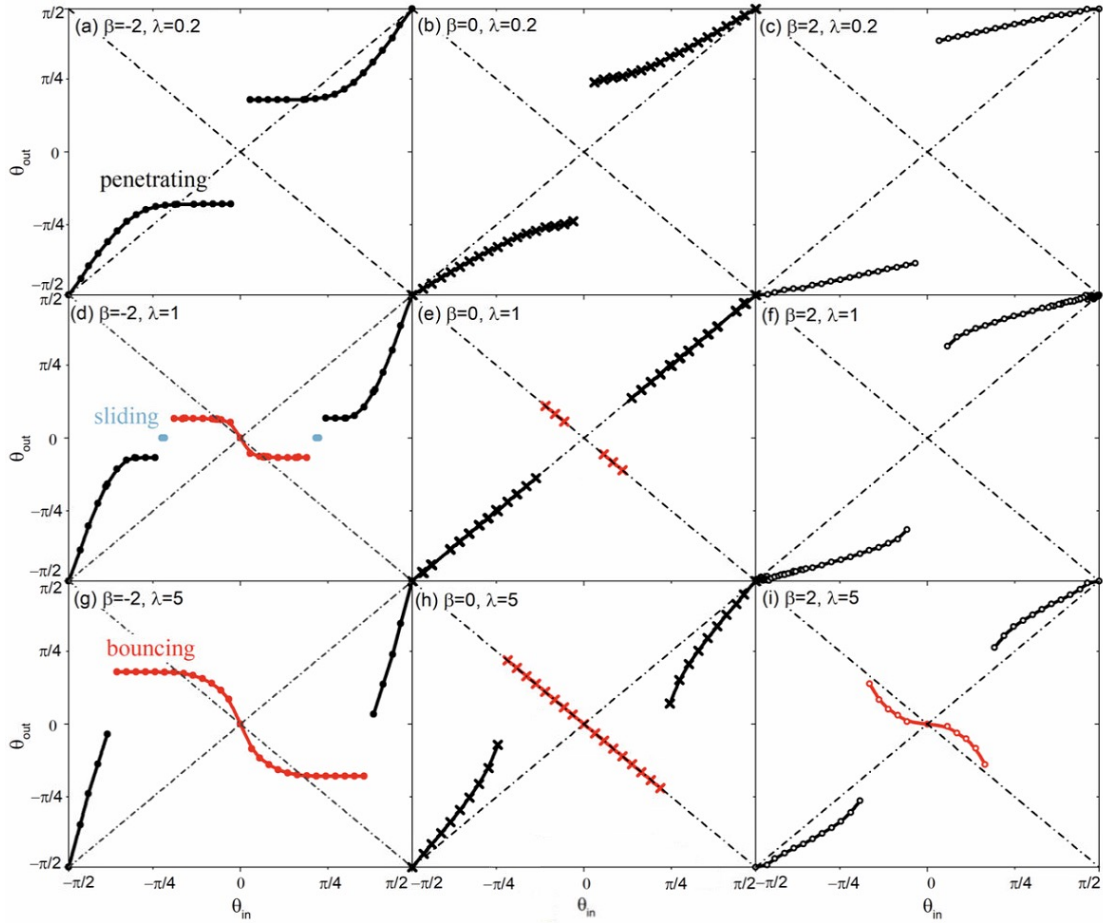
Figure 3.3. Changes in the orientation angle θ for different viscosity ratios (a)–(c) $\lambda = 0.2$; (d)–(f) $\lambda = 1$; (g)–(i) $\lambda = 5$ with swimmers with various swimming types $\beta = -2$, 0 and 2 after a single collision with the interface. This corresponds to a one-to-one mapping from θ_{in} to θ_{out}.

corresponding to a swimmer starting in the lower viscosity fluid, the bouncing mode dominates. Thus, we infer that the viscosity gradient will tend to propel swimmers towards regions of low viscosity and, the swimmers will exhibit a form of viscotaxis, with a preference for the low-viscosity fluid. Finally, for strong pullers at small initial angles, a new dynamical "hovering" mode emerges, while strong pushers still exhibit sliding motion. These results are summarized in Fig. 3.2(e) and (f), for $\lambda = 5$ and 10.

We further investigate the effect of the viscosity ratio λ on the swimmer's collision dynamics, by computing the map f relating the initial angle θ_{in} to the outgoing angle θ_{out}, after a single collision with the interface. These collision maps are presented in Fig. 3.3, for $\beta = -2, 0, 2$ swimmers and viscosity ratios $\lambda = 0.2, 1, 5$. Except for the
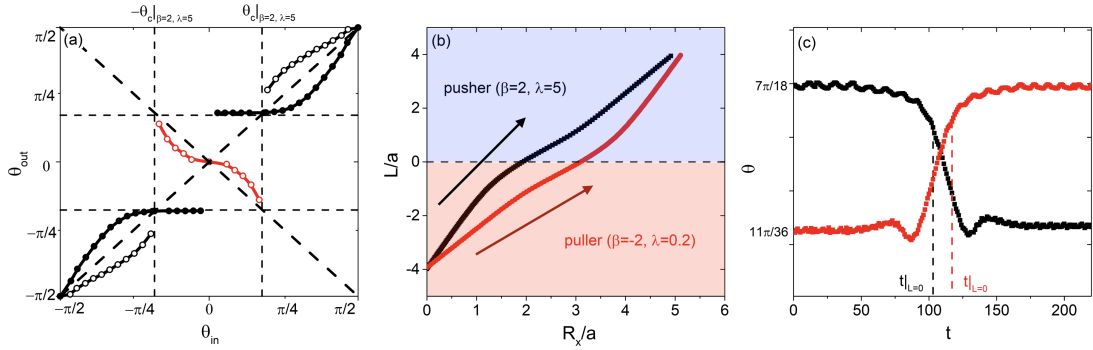
50

Figure 3.4. (a) Collisions maps, providing the change in the orientation angle θ for a puller ($\beta = 2$) at $\lambda = 5$ and a pusher ($\beta = -2$) at $\lambda = 1/5$, marked by empty and filled circles, respectively. The black symbols represent the penetrating motion, red symbols the bouncing motion. (b) The particle trajectory and (c) the time evolution of the orientation angle θ, for swimmers initially located at $L_{t=0} = -4a$. The pusher with $\beta = -2$, $\theta_{in} = 7\pi/18$, and $\lambda = 5$ is marked in black, while the puller with $\beta = 2$, $\theta_{in} = 11\pi/36$, and $\lambda = 1/5$ is marked in red.

bouncing motion of the neutral particles, which is absent for $\lambda = 0.2$ and extends over a wider range of incoming angles for $\lambda = 5$, the maps for $\lambda \neq 1$ exhibit clear deviations compared to the isoviscous results ($\lambda = 1$). To illustrate this, consider the effect of λ on the collision dynamics of pushers ($\beta = -2$). Compared with the isoviscous system, shown in Fig. 3.3(d), the threshold angle $|\theta_c|$ dividing the bouncing and penetrating behaviours shifts to larger values when the swimmer is initially in the low-viscosity fluid (i.e., $\lambda = 5$), as shown in Fig. 3.3(g). Furthermore, the outgoing angle θ_{out} for the penetrating/bouncing motion shows an overall decrease or increase depending on the viscosity ratio. This effect is particularly obvious for the penetrating motion, where the outgoing angle magnitude will be smaller than for the isoviscous case for the same initial angle θ_{in}. The opposite trends are observed for swimmers initially located in the higher viscosity fluid ($\lambda = 0.2$), as shown in Fig. 3.3(a).

Similar to the isoviscous case, where the pusher/puller duality is evident in the symmetry of the $\theta_{in} - \theta_{out}$ map and the particle trajectories at equal swimming strength $|\beta|$, the results for mismatched viscosities also show a clear symmetry, despite the strong influence of λ on the motion of the swimmer near the interface. We first focus on the penetrating motion, because this was the mode that most clearly evidenced this

51

symmetry for $\lambda = 1$. For a single penetrating process, the trajectories and angular changes mirror each other. To illustrate this, we compare the map $f : \theta_{\text{in}} \to \theta_{\text{out}}$ for swimmers with $\beta = \pm 2$, as shown in Fig. 3.4(a). The mapping for the penetrating motion f_p is symmetric about diagonal $\theta_{\text{out}} = \theta_{\text{in}}$. That is, the mapping for the pusher is the inverse of the mapping for the corresponding puller, under an inversion of the viscosity ratio, such that $f_p|_{\beta=-2,\lambda=1/5} = f_p^{-1}|_{\beta=2,\lambda=5}$. The threshold angle that divides the bouncing and penetrating motion for the pusher θ_c is equal to the maximum outgoing angle for the puller. To illustrate this, we consider pushers ($\beta = -2$) with $\theta_{\text{in}} = 7\pi/18$ at $\lambda = 5$, and pullers ($\beta = 2$) with $\theta_{\text{in}} = 11\pi/36$ at $\lambda = 0.2$ as representative examples. Both swimmers are initially set at $L_{t=0} = -4a$. According to Fig. 3.4(b), the trajectory of the puller (pusher) before it reaches the interface $L/a < 0$, is the same as the trajectory of the pusher (puller) after it leaves the interface. As expected, this symmetry is also evident in the evolution of the orientation angle, as shown in Fig. 3.4(c). This behaviour is seen for all swimmer types. In summary, the penetrating motion for pushers (pullers) at viscosity ratio λ, is the inverse of the penetrating motion for pullers (pushers) at viscosity ratio $1/\lambda$, such that $f_p|_{\beta,\lambda} = f_p^{-1}|_{-\beta,1/\lambda}$. When $\lambda = 1$, we recover the results of our previous work, $f_p|_{\beta,\lambda=1} = f_p^{-1}|_{-\beta,\lambda=1}$ [85].
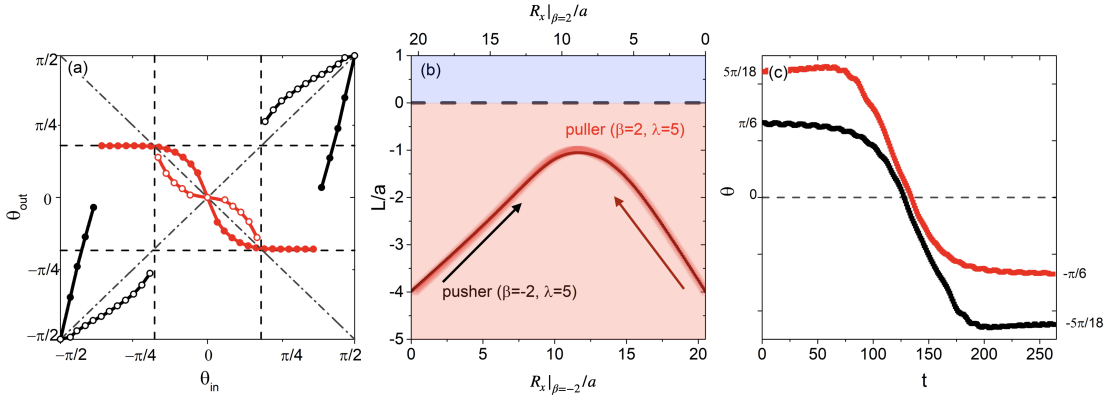
Figure 3.5. (a) Collision maps, providing the change in the orientation angle θ for a puller ($\beta = 2$) and a pusher ($\beta = -2$) at $\lambda = 5$, marked by empty and filled circles respectively; (b) the particle trajectory and (c) the time evolution of the orientation angle θ for swimmers initially located at $L_{t=0} = -4a$. The pusher ($\beta = -2$) with $\theta_{\text{in}} = \pi/6$ is marked in black, while the puller ($\beta = 2$) with $\theta_{\text{in}} = 5\pi/18$ is marked in red.

We now consider the bouncing motion of pushers and pullers. In view of the observations

52

Figure 3.6. (a) The particle trajectory and (b) the time evolution of the orientation angle θ, for neutral particles ($\beta = 0$) at $\lambda = 1$, 5 and 10. All swimmers are initially located at $L_{t=0} = -4a$, with orientation $\theta_{\text{in}} = \pi/12$.

that a wide variety of swimmer orientations will result in penetration of the interface when the swimmers are moving into the low-viscosity fluid ($\lambda < 1$) and that the pullers tend to penetrate at $\lambda = 1$, we will focus on $\lambda > 1$. According to Fig. 3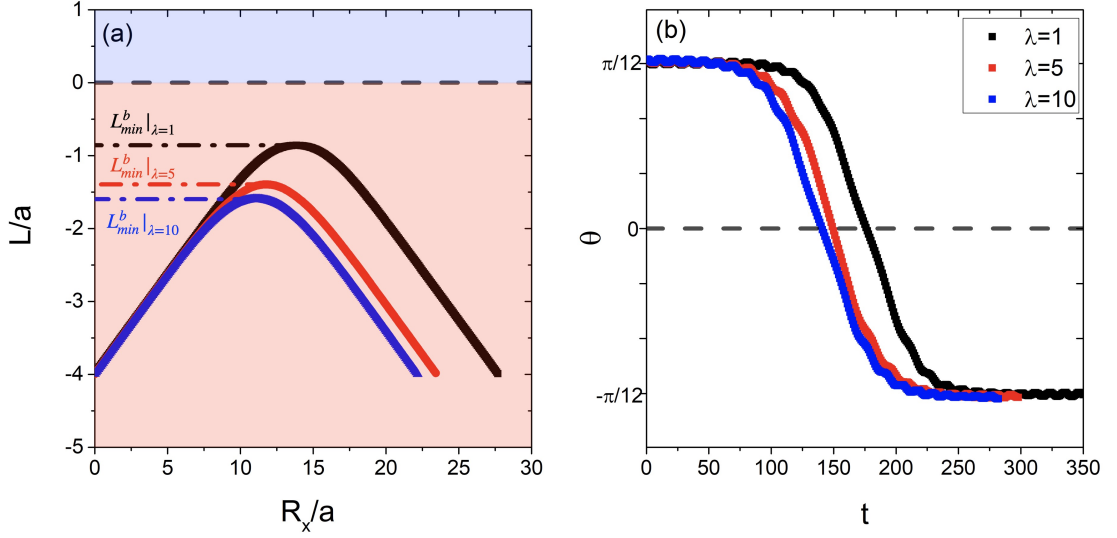.5(a), the mapping for the bouncing motion f_b of swimmers $\beta = \pm 2$ at a high viscosity interface ($\lambda = 5$) is symmetric about the diagonal $\theta_{\text{out}} = -\theta_{\text{in}}$. Thus, the pusher/puller duality can be expressed as $f_b|_{\beta,\lambda} = -f_b^{-1}|_{-\beta,\lambda}$. This can be seen by comparing the results obtained from simulations of a single bouncing process, i.e., a pusher ($\beta = -2$) with $\theta_{\text{in}} = -\pi/6$ and a puller ($\beta = 2$) with $\theta_{\text{in}} = -5\pi/18$, both under $\lambda = 5$. The time-evolution of the particle positions and orientations for this process are shown in Fig. 3.5(b) and 3.5(c). The pusher/puller trajectories are mirror images of each other, resulting from the time reversibility at a low Reynolds number. That is, the trajectory for the bouncing motion of a pusher (puller) corresponds to the (time-reversed) bouncing motion of a puller (pusher).

The bouncing motion for neutral particles, corresponding to the red curves in Fig. 3.3(e) and 3.3(h), is particularly interesting in how insensitive it is to λ, in contrast to pushers/pullers. Even though the threshold angle θ_c is seen to increase upon increasing

53

λ, the outgoing angle θ_{out} is always equal in magnitude to the approaching angle θ_{in}, regardless of the viscosity ratio λ. This represents a special case of the bouncing map obtained for pushers/pullers, $f_b|_{\beta,\lambda} = -f_b^{-1}|_{-\beta,\lambda}$, with $\beta = 0$. In order to further validate this observation, we conducted a series of simulations for neutral particles with various fluid viscosity ratios $\lambda = 0.1$, 0.2, and 1. The particles initially approach the interface with $\theta_{\text{in}} = \pi/12$. The effect of the viscosity is evident in the distance of the shortest approach to the interface $|L^b_{\text{min}}|$, which decreases with decreasing λ, as shown in Fig. 3.6(a). This indicates that the particle is sensitive to the viscosity gradient, and that a larger change in viscosity results in longer-range interactions, which allow the particle to start its reorientation process to escape the interface earlier, as shown in Fig. 3.6(b).

Finally, for strong pullers, we have observed a new "hovering" mode, different from the penetrating, bouncing, or sliding motions. To study this motion, we conducted simulations for puller with $\beta = 4$, at various approaching angles $\theta_{\text{in}} = \pi/9$, $\pi/12$, $\pi/18$ and $\pi/36$, with all particles initially located at $L_{t=0} = -4a$. The swimmer approaches the interface, initially turning towards it, while showing oscillations in its direction of motion. The swimmer then partially turns away from the interface, with increased oscillations in its orientation, before settling into the hovering motion, moving parallel to the interface at a fixed distance [see Fig. 3.7(a)]. We note that the orientation of the swimmer is not completely aligned with the interface. It is always pointing towards the interface, with a positive throughout the entire process, as shown in Fig. 3.7(b). Taking the dynamics of the puller ($\beta = 4$), with initial angle $\theta_{\text{in}} = \pi/9$, for $\lambda = 10$ as a reference [see Fig. 3.7(c)], we can clearly see that the orientation of the swimmer and its direction of motion are not parallel. In contrast to these pullers, strong pushers will show a sliding motion, in which they are adsorbed to and swim along the interface [85].
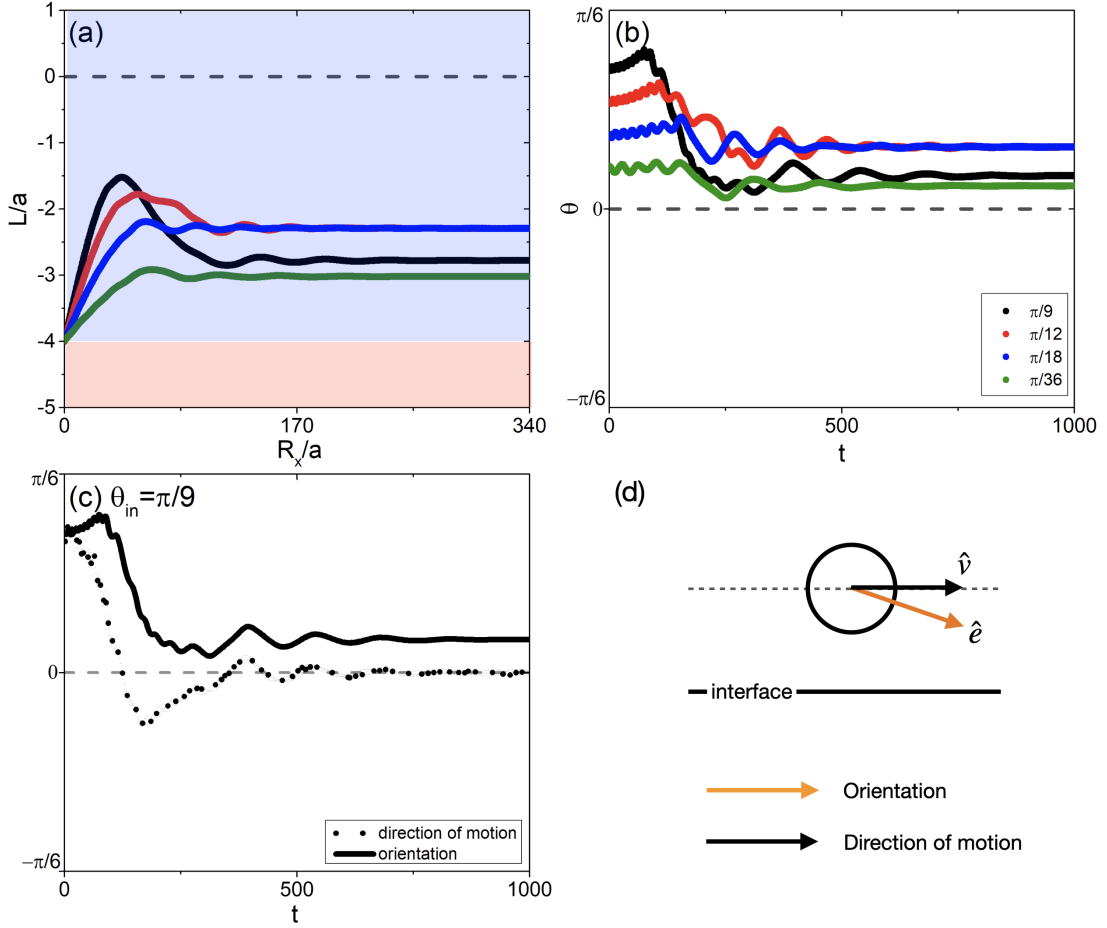
Figure 3.7. The new dynamical mode of "hovering motion results in particles swimming in the low-viscosity fluid parallel to the interface without touching it. (a) The particle trajectories are shown as well as (b) the time evolution of the orientation angle θ for pullers ($\beta = 4$) at $\lambda = 10$ for various approach orientations θ_{in}, with the swimmers initially located at $L_{t=0} = -4a$; (c) Shows the time evolution for θ (solid line) and φ (dotted line), i.e., the orientation and direction of motion, respectively, for a puller ($\beta = 4$) at $\lambda = 10$, with $\theta_{in} = \pi/9$. (d) Graphical illustration of the swimming state for a strong puller in a typical hovering motion.

3.4   Discussion

We have studied the effect of a viscosity ratio in binary phase-separated fluid mixtures on the dynamics of swimmers near the interface. In order to rule out the possibility that such dynamics are due to inertial effects, we also conducted simulations with a smaller Reynolds number by decreasing the velocity of swimmers. The trajectories are the same which indicates that the inertial effects are negligible in our present simulations.

we notice that swimmers show a preference towards the lower viscosity fluid. If one

considers an ensemble of swimmers, with a variety of incidence angles, the effect of the viscosity gradient will be to propel swimmers towards regions of low viscosity. This will tend to result in an enrichment of swimmers in the low-viscosity fluid. This type of viscotaxis is consistent with previous theoretical investigations on swimmers in viscosity gradients [63, 86–89]. These studies showed that a squirmer in a weak viscosity gradient will reorient in the direction of the lower viscosity region (negative viscotaxis), regardless of the swimming mode. This effect has been confirmed in experiments, such as the puller-like alga *Chlamydomonas reinhardtii*, which was observed to accumulate in low-viscosity zones at sufficiently strong gradients. [90–94]

We observe a new mode of motion for strong pullers which we refer to as "hovering". This mode was not observed for swimmers in fluids of equal viscosity. A similar mode has been reported in previous work that focused on pullers near a wall, rather than a deformable fluid-fluid interface at finite λ [54, 57, 75–77]. Although it is difficult to make a direct comparison with our work, the dynamics previously reported for pullers near rigid walls are similar to the hovering motion we observe. In both their work and ours, strong pullers first exhibit oscillating motion before eventually swimming parallel to the interface at a constant separation, maintaining an orientation tilted towards the interface (i.e., the particle orientation is not aligned with the direction of motion). Some understanding of this similarity can be obtained by noting that a solid wall can be regarded as a fluid-fluid interface in the limit $\lambda \to \infty$. Furthermore, for the hovering motion, the swimmers remain in the host (low viscosity) fluid, with the distance of the closest approach increasing as the viscosity ratio λ increases. Thus, the interaction with the interface can be expected to be well represented by the far-field approximations used in previous studies [54].

3.5   Conclusions

In this work, we have analyzed the dynamics of swimmers approaching a fluid-fluid interface between phase-separated fluids with distinct viscosities. The viscosity ratio λ, together with the swimming mode β (pusher or puller), determine the outcome of collisions of the swimmer with the interface. Such collisions are shown to give rise to four distinct dynamic modes: bouncing, sliding, penetrating and hovering. Compared with the results obtained for isoviscous systems $\lambda = 1$, we observe that the swimmer exhibits a preference towards the lower viscosity fluid (i.e., viscotaxis). This preference should be understood in the sense that, for a wide distribution of contact angles, more swimmers will transition into the low viscous environment than vice-versa. This means that a typical swimmer, drawn from this distribution, that starts in a low viscosity fluid is more likely to bounce back (reflect) at the interface, while a swimmer starting in the high viscosity fluid is more likely to penetrate the interface and swim into the lower viscosity fluid. Even though the outgoing angle θ_{out} for the penetrating/bouncing motion is mainly determined by the swimming type β and the initial angle θ_{in}, the precise functional dependency depends on the viscosity ratio λ. A duality between pushers/pullers can be clearly seen in the trajectories for penetrating and bouncing swimmers. In addition, we observed that strong pullers, initially located in the lower viscosity fluid, can exhibit a new type of hovering motion, moving parallel to the interface at a fixed distance $|L|/a > 1$, which is not observed for isoviscous systems.

Our study represents a detailed analysis of the role played by the viscosity ratio on the dynamics of swimmers near an interface. This improves our understanding of swimming in complex fluid environments and may help with the interpretation of similar physiological and biological phenomena. Further developments of this work may allow a numerical investigation of more complex interfacial structures, such as curved interfaces, e.g., swimming near a spherical or tubular domain.

3.6 Appendix

3.6.1 Software

All simulations presented in this chapter were conducted using the open-source version of the KAPSEL DNS software. KAPSEL has been developed in our lab to simulate the dynamics of solid particles dispersed in complex fluids. Detailed descriptions of KAPSEL are available online [67].

Chapter 4

Dynamics of a model microswimmer near a liquid droplet with a penetrable interface

4.1 Introduction

Microorganisms in viscous fluids are known to swim in complex trajectories with the presence of boundaries. For example, the circular motion, observed in experiments with *E. Coli*, is that the microswimmers may swim in large circles clockwise when they are near a solid-fluid boundary, and in circles of opposite handedness near an air-fluid surface [78, 80]. Researchers believe that these near-surface phenomena are of utmost importance and may lead to the formation and evolution of biofilms [95–97]. A depth understanding of microbial motion in varied environments can also be sought by conducting experiments on artificial microswimmers, which provide greater control over their swimming behaviour [98–101]. These artificial swimmers have indeed been

used to study the intricacies of locomotion near the boundaries. Takagi *et al.* [102] performed one such study on the locomotion of a Janus micro-rod in the vicinity of inert colloidal particles. Their experiments revealed that the rod got trapped near the surface of a colloid, and orbited around it for some time, before escaping and progressing toward similar interactions with other colloids encountered in its path. This behaviour was explained using lubrication theory and steric interactions. Later, several theoretical analysis of a microswimmer near a colloid/drop has been reported [103–105]. However, the vast majority of these mathematical models only consider far-field hydrodynamics, while the near field is simplified by approximating the colloid/drop as a rigid sphere.

On the other hand, a physical model for binary fluid mixtures containing a penetrable soft interface has been proposed in our previous work, which allows the numerical studies to be no longer restricted to the far-field approximation [85]. These previous studies have revealed that microswimmers can be strongly influenced by the interface; they may have several distinct dynamical modes, such as penetrating, sliding, bouncing, and paralleling motions, when they approach the planar interface. These dynamical modes depend on the both swimmer's properties, e.g., approaching angle, swimming type and etc., and the fluid's properties, such as viscosity ratio.

In this chapter, we aim to extend our research to the locomotion of microswimmers near a drop that has a soft, deformable, penetrable but non-planar surface. A study of this kind is particularly relevant to the phenomenon of biodegradation of oil drops by marine bacteria in the event of an oil spill [106, 107]. For example, in the Deepwater Horizon oil spill, it is well known that marine bacteria play an important role in the degradation of the contents of the spill (both water soluble and insoluble) [108–111]. During this degradation process, bacteria are retained in the oil droplets which act as a rich source of carbon. A purely hydrodynamics-driven attraction of swimmers to oil drops hints at an intriguing passive mechanism through which motile marine bacteria may forage for nutrition amongst oil droplets. Towards this end, we aim to analyze the dynamics of a

microswimmer in the vicinity of a drop and bring out the variation in the swimmer's and fluid's properties.

This chapter is organized as follows. We first review our mathematical model, including the governing equations of swimmer motion and fluid flow, and the binary fluid conditions for a droplet. We then process to solve for the dynamics of the swimmer and define the critical trapping radius in the case of the sliding motions. Finally, we perform a comparative analysis to pinpoint the influence of swimming types and viscosity ratios. In the end, we conclude by reiterating our results and discussing them with regard to biodegradation.

4.2   Simulation Methods

4.2.1   The squirmer model

In this work, the squirmer model is used to describe the swimmers [32, 50]. Squirmers are particles with modified stick boundary conditions at their surface which are responsible for the self-propulsion. The general form is given as an infinite expansion of both radial and tangential velocity components, but for simplicity, the azimuthal and radial terms are usually neglected and the infinite sum is truncated to second order [34, 35]. For spherical particles, the surface velocity is given as

$$\boldsymbol{u}^s(\vartheta) = B_1(\sin\vartheta + \frac{\beta}{2}\sin 2\vartheta)\hat{\boldsymbol{\vartheta}}, \qquad (4.1)$$

where $\hat{\boldsymbol{\vartheta}}$ is the tangential unit vectors for a given point at the surface of the particle. $\vartheta = \cos^{-1}\hat{\boldsymbol{r}} \cdot \hat{\boldsymbol{e}}$ is the polar angle between radial unit vectors $\hat{\boldsymbol{r}}$ and the squirming direction $\hat{\boldsymbol{e}}$. The coefficient of the first term in Eq. (4.1), B_1, determines the steady-state swimming velocity of the squirmer $U_0 = 2/3B_1$. The coefficient of the second mode, B_2, determines the stress exerted by the particles on the fluid. The ratio of the

first two modes $\beta = B_2/B_1$ determines the type and strength of the swimming. When β is negative, the squirmer is a pusher, which swims generating an extensile flow field, and when β is positive, the squirmer is a puller, which swims generating a contractile flow field. For the case when $\beta = 0$, we refer to the swimmer as a neutral swimmer which is accompanied by a potential flow.

4.2.2   Smoothed profile method for binary fluids

In order to solve the dynamics of squirmers swimming in an immiscible binary A/B fluid system, while fully accounting for the hydrodynamic interactions, the coupled equations of motion for the solid particles and the component fluids within the model H representation, i.e., the Newton-Euler and Cahn-Hilliard Navier-Stokes equations, need to be considered [44, 45].

Furthermore, to couple these equations efficiently, we have used the Smooth Profile (SP) method [36], in which the A/B fluid and solid particle phases can be defined in terms of order parameters ψ_A, ψ_B, and ϕ. In the SP method, all sharp particle boundaries, including solid/fluid and fluid/fluid boundaries, are replaced by diffuse interfaces of finite thickness ξ, and thus allows us to easily couple the rigid-body dynamics to the dynamics of the (phase-separating) fluids. In what follows we briefly describe how to solve for the (coupled) rigid-body dynamics, phase-separating dynamics, and fluid dynamics. Detailed descriptions of the SP method and its implementation can be found in our earlier publications.[36, 38–40]

4.2.2.1 Particle dynamics

The position, velocity and angular velocity of particle i are expressed as $\boldsymbol{R}_i$, $\boldsymbol{V}_i$ and $\boldsymbol{\Omega}_i$. The time evolution of the particles follows from the Newton–Euler equations:

$$\dot{\boldsymbol{R}}_i = \boldsymbol{V}_i, \tag{4.2}$$

$$\dot{\boldsymbol{Q}}_i = \mathrm{skew}(\boldsymbol{\Omega}_i) \cdot \boldsymbol{Q}_i, \tag{4.3}$$

$$M_i \dot{\boldsymbol{V}}_i = \boldsymbol{F}_i^H + \boldsymbol{F}_i^C + \boldsymbol{F}_i^{ext}, \tag{4.4}$$

$$\boldsymbol{I}_i \cdot \dot{\boldsymbol{\Omega}}_i = \boldsymbol{N}_i^H + \boldsymbol{N}_i^{ext}, \tag{4.5}$$

where $\boldsymbol{Q}_i$ is the orientation matrix, M_i the masses, and $\boldsymbol{I}_i = 2/5 M_i a_i^2 \mathsf{I}$ (with a_i the radius of particles) the moments of inertia (I the unit tensor); $\mathrm{skew}(\boldsymbol{\Omega}_i)$ is the skew-symmetric matrix for the angular velocity $\boldsymbol{\Omega}_i$. The hydrodynamic forces and torques are given by $\boldsymbol{F}_i^H$ and $\boldsymbol{N}_i^H$, $\boldsymbol{F}_i^C$ represents direct particle–particle interactions ($\boldsymbol{N}_i^C = 0$), and $\boldsymbol{F}_i^{ext}$ and $\boldsymbol{N}_i^{ext}$ are the external forces and torques, respectively.

Within the SP method, the sharp solid-fluid interface is replaced by a diffuse one with finite thickness ξ_p, and the solid phase is accounted for via a smooth and continuous profile function $\phi(\boldsymbol{r})$, which takes a value of 1 in the solid domain, 0 in the fluid domain, and smoothly interpolates between the two domains across the interfaces.

4.2.2.2 Phase-separating dynamics

The order parameters, $\psi_A(\mathbf{r})$ and $\psi_B(\boldsymbol{r})$, are used to represent the volume fractions of fluid A and B respectively ($0 \leq \psi_\alpha \leq 1$). Coupled with the order parameter ϕ for the solid domain, the sum total of the volume fraction of all components (fluids and particles) is constrained to be unity,

$$\psi_A + \psi_B + \phi = 1, \tag{4.6}$$

then the proportion of each fluid can be given by a single order parameter $\psi(\boldsymbol{r})$,

$$\psi = \psi_A - \psi_B. \tag{4.7}$$

This order parameter $\psi(\boldsymbol{r})$ takes a value of 1 in the A domain, and -1 in the B domain.

Since fluid A and B are immiscible, the dynamics for $\psi(\boldsymbol{r})$ is determined by the following modified Cahn-Hilliard equation

$$\frac{\partial \psi}{\partial t} + (\boldsymbol{u} \cdot \boldsymbol{\nabla})\psi = \kappa \nabla^2 \mu_\psi, \tag{4.8}$$

where $\boldsymbol{u}$ is the total velocity field, and κ the mobility coefficient. $\mu_\psi = \delta\mathcal{F}/\delta\psi$ is the chemical potential, derived from the Ginzburg-Landau (GL) free energy function $\mathcal{F}$. Since we assume that the particles will interact with the interface purely hydrodynamically, GL free energy function can be given by

$$\mathcal{F}[\psi, \phi] = \int \mathrm{d}\boldsymbol{r} \left[f(\psi) + \frac{\alpha}{2}(\boldsymbol{\nabla}\psi)^2 \right] \tag{4.9}$$

The first term in the integrand of Eq. (4.9), $f(\psi) = \frac{1}{4}\psi^4 - \frac{1}{2}\psi^2$ represents the Landau double-well potential, with two minima at $\psi = 1$ and -1, and the second term is the potential energy associated with the fluid A/B interface. Then the chemical potential for order parameter ψ is

$$\mu_\psi = f'(\psi) + \alpha\nabla^2\psi, \tag{4.10}$$

and the chemical potential for the fluid-particle interactions $\mu_\phi = \delta\mathcal{F}/\delta\phi$ is equal to 0.

4.2.2.3 Fluid dynamics

A total velocity field, $\boldsymbol{u}$, which includes both the fluid and particle velocities, is defined as

$$\boldsymbol{u} = (1 - \phi)\boldsymbol{u}_f + \phi\boldsymbol{u}_p, \tag{4.11}$$

$$\phi\boldsymbol{u}_p = \sum_i \phi_i[\boldsymbol{V}_i + \boldsymbol{\Omega}_i \times \boldsymbol{R}_i] \tag{4.12}$$

where $(1 - \phi)\boldsymbol{u}_f$ is the contribution from the fluid, $\phi\boldsymbol{u}_p$ from the particle. Then, the time evolution of this total flow field $\boldsymbol{u}$ obeys:

$$\rho(\partial_t + \boldsymbol{u} \cdot \boldsymbol{\nabla})\boldsymbol{u} = \boldsymbol{\nabla} \cdot \boldsymbol{\sigma} + \rho(\phi\boldsymbol{f}_p + \boldsymbol{f}_{sq}) \tag{4.13}$$

$$- \psi\boldsymbol{\nabla}\mu_\psi - \phi\boldsymbol{\nabla}\mu_\phi,$$

$$\boldsymbol{\nabla} \cdot \boldsymbol{u} = 0 \tag{4.14}$$

where $\phi\boldsymbol{f}_p$ is the body force necessary to maintain the rigidity of particles, and $\phi\boldsymbol{f}_{sq}$ is the force due to the active squirming motion. $\boldsymbol{\sigma}$ in Eq. (4.13) is the Newtonian stress tensor, defined in terms of the total fluid velocity as

$$\boldsymbol{\sigma} = -p\mathsf{I} + \eta[\boldsymbol{\nabla}\boldsymbol{u} + (\boldsymbol{\nabla}\boldsymbol{u})^T] \tag{4.15}$$

The phase-dependent viscosity η, consisting of the viscosity of fluids A, fluid B, and the particle domains, which are donated by η_A, η_B, and η_p respectively, is defined as

$$\eta(\boldsymbol{r}) = \eta_A\psi_A(\boldsymbol{r}) + \eta_B\psi_B(\boldsymbol{r}) + \eta_p\phi(\boldsymbol{r}) \tag{4.16}$$

$$= \eta_A\left(\psi_A(\boldsymbol{r}) + \lambda\psi_B(\boldsymbol{r})\right) + \eta_p\phi(\boldsymbol{r}),$$

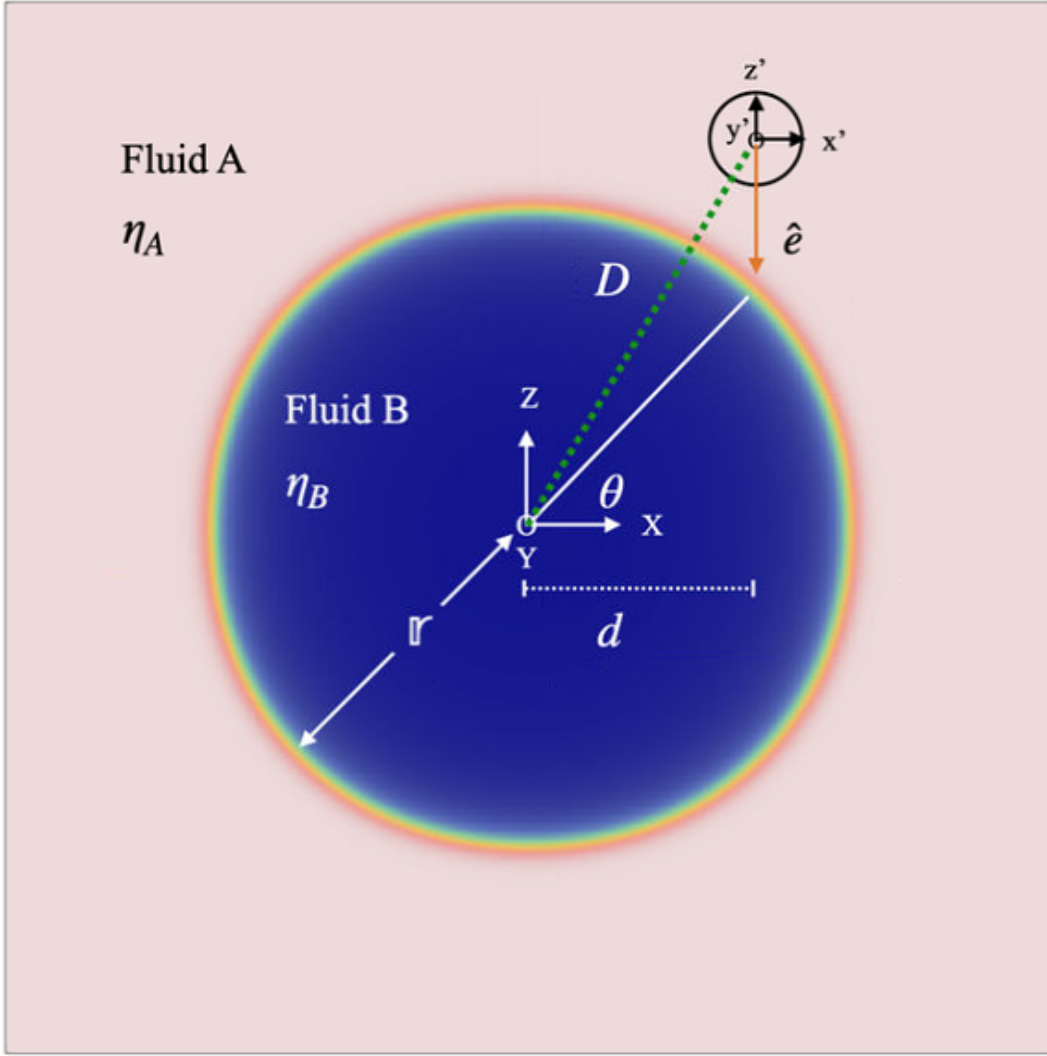where $\lambda = \eta_B/\eta_A$ is the fluid viscosity ratio.

Figure 4.1. Illustration of the drop/swimmer system. The drop with its radius r, consisting of fluid B, is located at the centre of the system, and the swimmer with its radius a is initially located in the host fluid A.

4.2.3 System parameters

Using the calculation method presented above, we conducted three-dimensional direct numerical simulations (DNS) of microswimmer near drops.

A schematic illustration of the swimmer/drop system is given in Fig. 4.1. The radius a of the swimmer is set to be $a = 4\Delta$, and solid-fluid interface thickness ξ_p is 2Δ, where Δ stands for the grid spacing. Regarding the parameters in Eq. (4.1), we set $B_1 = 0.015$ for all the calculations and varied β to investigate the β dependency of the

dynamics in section 4.3.1. The simulation system is set up as a square with sides of 256Δ mainly consisting of fluid A as the host fluid. Periodic condition is applied. The droplet, consisting of fluid B, is set right in the centre of the square. The drop keeps its spherical shape with the minimum interface area between fluids A and B which results in relatively low free energy. The radius of the drop r is varied from 16Δ to 80Δ to study the r dependency of the dynamics in section 4.3.2. The distance between the centre of the swimmer and the drop is donated by D. d is the distance between the centre of the swimmer and the drop in $\hat{\boldsymbol{x}}$ axis. The collision angle θ is defined as $\cos\theta = d/\mathrm{r}$.

We also conduct the simulation of swimmers near the drop with $\mathrm{r} = 80\Delta$ in which the system domain is enlarged by a factor of two. The results show no significant difference which means the self-interactions resulting from the periodic domains can be ignored in this chapter.

4.3 Results

4.3.1 Swimming motions

To examine the motions of microswimmers near the drop, we first conduct a series of simulations for different swimmers with different collision angles θ. The radius of the drop r is set to 66Δ.

Three kinds of motion are observed, as illustrated in Fig. 4.2. In case (i), the swimmer passes through the surface into the droplet after interacting with the surface domain with $D < \mathrm{r}$, as shown in Fig. 4.2(a) and Fig. 4.3. In case (ii), once the swimmer reaches the drop surface, it gets trapped and begins to orbit the drops [see Fig. 4.2(b)] with $D = \mathrm{r}$, as shown in Fig. 4.3. In case (iii), an approaching swimmer simply skims the drop surface for some time [see Fig. 4.2(c)], either long or short, then escapes with $D > \mathrm{r}$. However, these three swimming modes (i)–(iii) well match the dynamics of swimmers near a planar interface in our previous work, which were named "penetrating", "sliding"
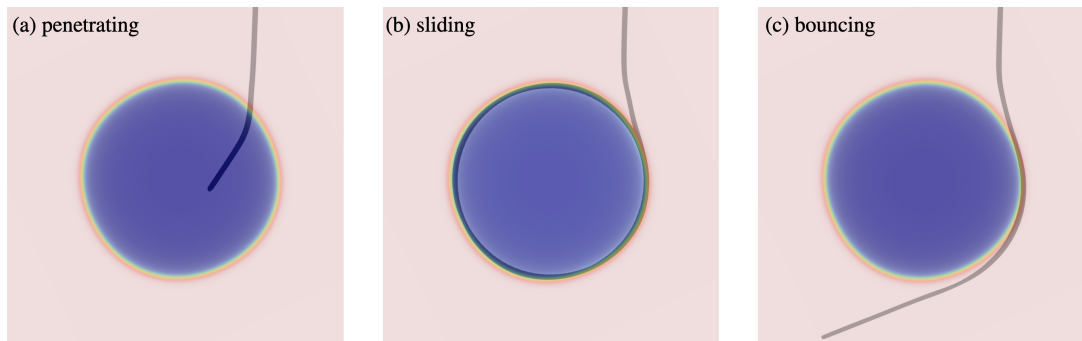
Figure 4.2. Trajectories of different swimmers with (a)$\beta = 2$, (b)$\beta = -7$, (c)$\beta = -5$ once reaching the surface of the drop with its radius $r = 16.5a$ (a is the radius of the particle), correspond to three swimming motions respectively.

Figure 4.3. The time evolution of the distance between the centre of the drop with its radius $r = 16.5a$ and different swimmers with $\beta = 2, -5$, and -7 which swim in penetrating, bouncing and sliding motions, respectively, and are marked in different colours.

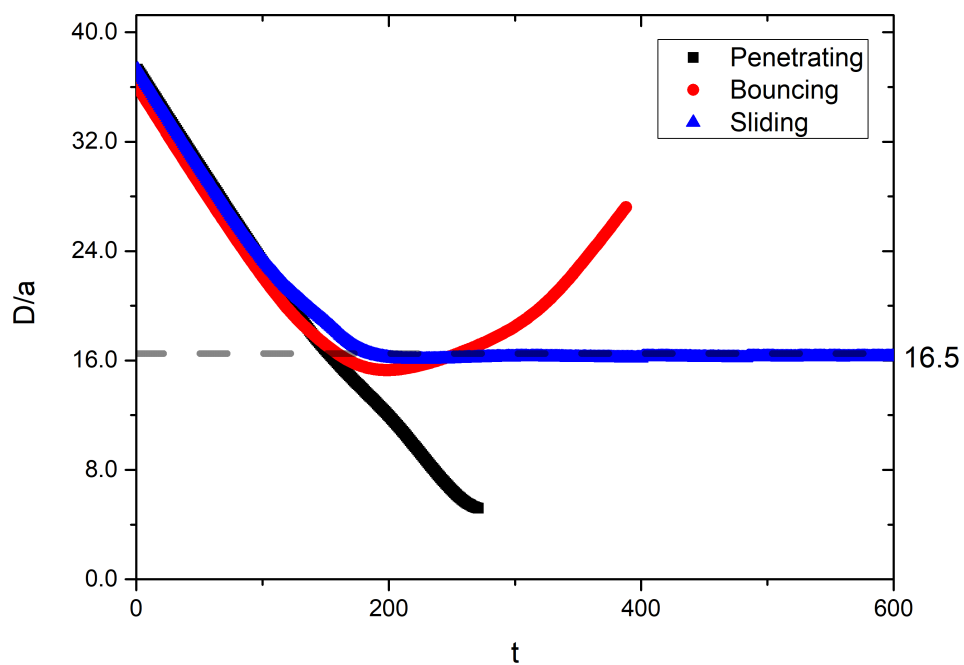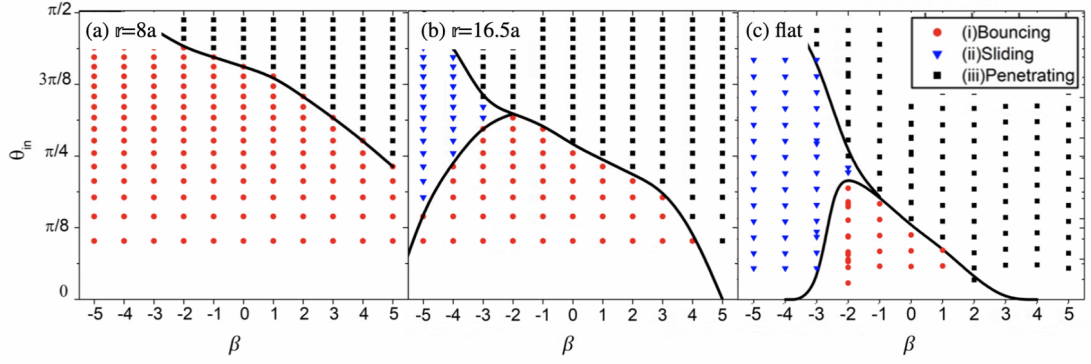Figure 4.4. Phase diagram for swimmers with various β value (a)near the drop with $r = 8a$; (b) near the drop with $r = 16.5a$; (c) near the planar interface, reproduced. a is the radius of the droplet.

and "bouncing" motions respectively. We think this is because planes can likewise be considered as the surface of droplets with infinite radius $r = \infty$. Thus, in this work we decide to use the same names, i.e., (i) "penetrating", (ii) "sliding", and (iii) "bouncing" motions.

In order to investigate the impact of interfacial geometry, we make a comparison with the dynamics of swimmers near the planar interface. In general, the dependency of the collision angle on these three motions is similar. For the relatively weak swimmers, if the collision angle θ_{in} is small, the swimmer will swim along the interface for a distance and then escape from it. If θ_{in} is large, the swimmer is able to swim into the drop. For relatively strong swimmers, the strong pusher gets trapped and orbits the surface of the droplet while the strong puller prefers to penetrate the surface. However, some differences still exist, as shown by the fact that swimming patterns can be different for the same microswimmers with the same collision angle. According to Fig. 4.4, we note that as the droplet radius increases, the bouncing cases decrease significantly. Meanwhile, the penetrating and sliding cases increase. Even in the case of the droplet with $r = 8a$, the sliding motion is not observed. Thus, we consider that the droplet radius has a strong effect on the dynamics near the surfaces of the drop.

We are also interested in the effect of the viscosity difference on the dynamic of swimmers near the drop. As shown in Fig. 4.5, with an increase in the value of λ, i.e, the ratio of
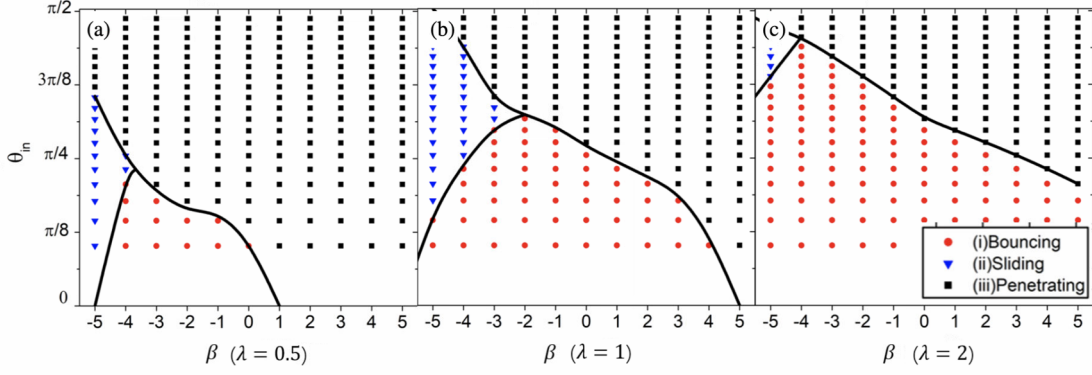
Figure 4.5. Phase diagram for swimmers with various β value near the drop with $r = 16.5a$, with the viscosity ratio (a)$\lambda = 0.5$, (b)$\lambda = 1$ and (c)$\lambda = 2$.

the viscosity of the liquid inside the droplet to the liquid outside the droplet, we note that the bouncing motion becomes dominant and the cases of the penetrating motion decreases. It shows that microswimmers prefer swimming in fluids with relatively low viscosity, and this conclusion is consistent with our previous research in **Chapter 3**.

4.3.2 Critical trapping radius

We think that there exists a critical trapping radius of the drop r_c, below which an approaching swimmer may simply skim the drop surface for some time before escaping or swimming into the drop, regardless of the collision angle θ. For radii larger than the critical trapping radius, the swimmer can be hydrodynamically trapped onto the drop surface and slide on the interface.

In order to explore the minimum critical radius r_c, we conduct a series of simulations in which different swimmers swim toward the drop with various radii r. Since this kind of trapping character is only observed for pushers, as shown in Fig. 4.4, we only conduct the simulations for pushers ($\beta < 0$). The collision angle varies from 0 to $\pi/2$ to check whether the swimmer has the ability to slide on the surface. As the result, Fig. 4.6 shows how the critical trapping radius for a drop, r_c, varies as a function of swimming strength β.

70
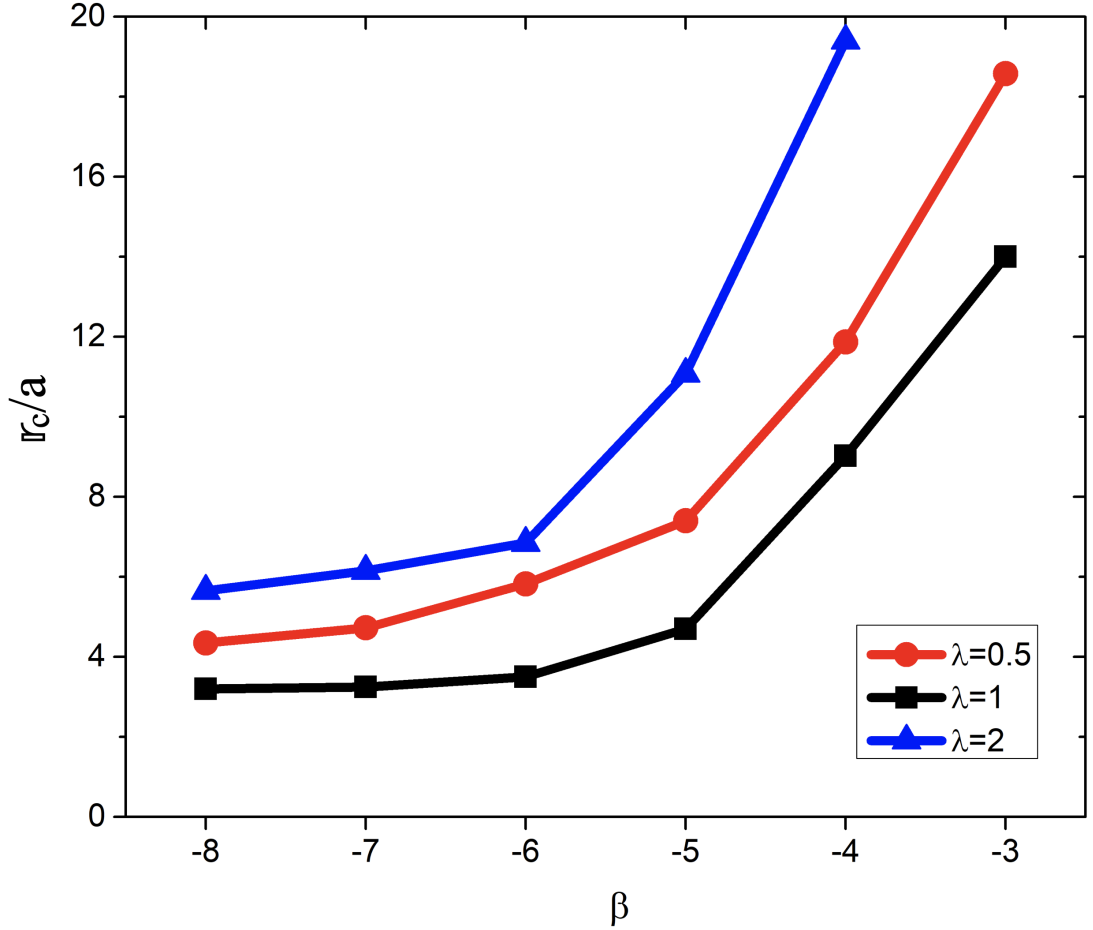
Figure 4.6. Variation of the critical trapping radius for drops with the swimmers' swimming strength β for different viscosity ratios $\lambda = 0.5, 1, 2$, marked in different colours and symbols.

According to Fig. 4.6, we note that the critical trapping radius $\mathbb{r}_c$ is highly correlated with the swimming strength β; weak pushers can orbit around the drop with a large radius, while strong pushers are said to be "more capable" in getting trapped. The critical trapping radius decreases with increasing swimming strength and shows a non-linear correlation.

The effect of viscosity ratio λ is also investigated in Fig. 4.6. We note that for the non-isoviscous system, whenever λ is not equal to 1, the critical trapping radius is greater than that for the isoviscous condition. We believe this is related to the nature that microswimmers have a preference for the low viscosity fluid, which is observed in our previous work. Therefore, when the viscosity of the fluid inside the droplet is lower than that of the fluid outside ($\lambda < 1$), swimmers prefer to swim into the drop in a penetrating

motion. Likewise, when the viscosity of the fluid inside the droplet is higher than that of the fluid outside ($\lambda > 1$), swimmers prefer to escape from the drop and swim back into the host fluid as a bouncing motion. Both of these two conditions are not conducive to the slide of particles on the droplet surface. Moreover, a significant difference in the value of r_c occurs for weak pushers, with the most viscous drops being less capable of trapping microswimmers that approach them directly.

4.4   Discussion

In this chapter, we further extend our study of the dynamics of microswimmers from cases of the planar interface to cases of the non-planar surface. Because of the penetrating nature of the interface, our study differs somewhat from previous studies on the dynamics near droplets. Many works also studied the trapping character of microswimmers near the drop surface [104, 105]. However, in their work, the far-field description they employed has been proven to be only accurate to distances as small as a few body lengths away from the surface. But the near-field dynamics were simply approximated as a hard-core repulsion. This approximation resulted in swimmers being rejected from penetrating the droplet surface. Thus, for some cases, such as pullers approach the drop or the viscosity of the fluid inside the drop is relatively low ($\lambda < 1$), the swimmers were reported to orbit the droplet surface with its squirming axis always pointing inside the droplet. They considered swimmers in such cases are trapped, whereas in our work swimmers usually penetrate the drop surface under such conditions.

With regard to the cases of biodegradation for oil droplets mentioned at the beginning of this article, we were surprised to find that both the non-planar surface and the viscosity difference make the hydrodynamic adhesion of microswimmers on the droplet surface more difficult. Also, the swimming type of microswimmers that can adsorb to the surface of the oil droplets is restricted to strong pushers. Furthermore, some work has reported that surfactants play an important role in this biodegradation, on the one hand

by dispersing the oil slick into fine droplets and increasing the contact area between oil and water, and on the other hand by improving the relative C:N:P ratio [112, 113]. However, according to our results, the former is not rigorous unless the drop radius is always larger than the capture radius. The latter, on the other hand, requires the chemical interaction of the liquid with the particles to be included in the model.

In addition, in order to rule out the possibility that the observed dynamics are due to inertial effects, we also conducted simulations with a smaller Reynolds number by decreasing the velocity of swimmers. We obtained equivalent trajectories, which indicates that the inertial effects are negligible in our present simulations.

4.5 Conclusions

In this chapter, we further investigate the dynamic of the microswimmer near the drop by extending to no-planar surfaces. Three motions, including penetrating, bouncing, and sliding motion, are observed once the swimmers reach the surface of the drop. Compared to the planar interface case, the radius of the droplet showed a further influence on the choice of swimming modes. The critical trapping angle r_c, the minimum radius that can make pushers get trapped and slide on the surface, is highly correlated with swimming strength, with a smaller radius for strong pushers and a larger radius for weak pushers. In addition, compared to isoviscous systems, both positive and negative viscosity differences between the fluids inside and outside the drop have a negative effect on this hydrodynamic adhesion.

Our study represents a detailed analysis of dynamics for microswimmers near the drop surface. It further improves our understanding of the dynamics of microswimmers in complex fluid systems and might allow for a more detailed study of similar physiological and biological phenomena, such as oil-microbe interactions in lab-on-a-chip setups or marine ecosystems.

Chapter 5

Concluding Remarks

5.1 Summary

This dissertation is devoted to the study of the dynamics of a model microswimmer near a liquid-liquid boundary by means of three-dimensional direct numerical simulation with fully resolved hydrodynamics. In order to fully understand such dynamics, we first developed a simple physical model in which swimmers interact with a soft, deformable, and penetrable interface in **Chapter 2**. In this chapter, we observed three distinct swimming modes for microswimmers after colliding with interfaces. We also explored the dependence of these swimming motions on the properties of swimmers, such as initial angles, swimming types, etc. Then in **Chapter 3** and **Chapter 4**, we add new variables and constraints to the physical model proposed earlier. The viscosity difference of fluids is considered in **Chapter 3** and the non-planar interface (droplet surface) in **Chapter 4**. In both of these chapters, the dynamics of microswimmers are compared to the simulations in which swimmers interact with the flat interface in an isoviscous system to understand the effect of each variable.

In **Chapter 2**, We first conduct a series of simulations in which a swimmer approaches the interface with different initial angles, to examine the motions of microswimmers near

an interface. In this chapter, we set the swimmer initially located in fluid A and make it swim towards fluid B. As a result, we clarified that three distinct swimming modes can be observed: bouncing motion in which the swimmer bounces back to the host fluid, sliding motion in which the swimmer slides on the interface, and penetrating motion in which the swimmer passes through the interfacial region separating the fluids and swim into the fluid B. In general, as for weak swimmers, the initial angle plays a dominant role in determining the nature of the motion at the interface. That is, the swimmer with a small initial angle will bounce back from the interface, whereas the one with a large initial angle will swim across the interface. Since the threshold angle dividing the bouncing and penetrating motions is different for different swimmers, together with the fact that strong swimmers exhibit a single sliding/penetrating motion that is not dependent on the approaching angle, we suspected that the swimmer type has a strong effect on the dynamics near fluid–fluid interfaces. To investigate the dependency of swimming type, we made a one-to-one mapping from approaching angles to outgoing angles for different swimmers. For weak swimmers, we found that when pushers and pullers start from the same initial angle and exhibit the same swimming mode (penetrating or bouncing), their orientation angles will change in opposite ways. In order to explain this pusher/puller duality, we measured the time evolution of the swimmer's orientation during the whole process. The sinusoidal dependence between the reorientation velocity and the orientation was confirmed. This result matched the work by Gidituri *et al.* well quantitatively, in which they investigated the reorientation dynamics of spherical microswimmers trapped at a fluid-fluid interface. On the other hand, when it comes to strong swimmers, strong pushers prefer to slide on the interface whereas strong pullers tend to swim perpendicular to the interface. Also, we extended our simulation from a single collision to repeated collisions with the interface, we observed three final steady states: penetrating the interface perpendicular to the interface for pullers, bouncing back and forth between two interfaces with a certain angle which is only related to swimming type for weak pushers, and sliding on the interface for strong pushers.

In **Chapter 3**, we extended our work to consider the dynamics of swimmers at the interface of two fluids with mismatched viscosities. We first introduced the phase-dependent order parameter for the viscosity field into the computational mode we have used in **Chapter 2**, and therefore can take the variable viscosity into account. Then, we analyzed the effect of the viscosity on the motion of the swimmer in the low Reynolds-number regime. As the result, in addition to the three modes ("bouncing", "sliding" and "penetrating") which we noted in **Chapter 2**, we also observed a new dynamical "hovering" mode, in which the swimmer tends to move parallel to the interface, at a fixed (non-zero) distance. By measuring the time evolution of the positions and orientations, we found that several sets of trajectories for the bouncing and penetrating motions exhibited time-reversal symmetry due to the pusher/puller duality. We also have summarised the relations for these types of symmetric, which can also recover cases in the isoviscous system. Moreover, compared to the isoviscous case, we found that the viscosity difference can significantly affect the dynamics during a collision with the interface, i.e., the relationship between incoming and outgoing angles. In addition, interestingly, by analyzing the swimmer dynamics in the hovering motion, we found that both the trajectories and the time evolution of the orientation are similar to those of swimmers near a solid wall.

In **Chapter 4**, the study was extended to non-planar interfaces by investigating the dynamics of microswimmers near droplets. In this chapter, we first performed simulations for swimmers approaching the drop. The swimming motions reported in our previous work are also observed, indicating that the dynamic of swimmers near the drop surface remained consistent with one near a flat interface. Next, we conducted simulations with different drop sizes. Compared to the planar interface cases, the radius of the droplet showed a further influence on the choice of swimming modes. Additionally, in this chapter, the dependence of the critical capture radius of the droplet on the properties of the microswimmers, such as swimming types and strength, was investigated. The results showed that only strong pullers are able to slide on the droplet surface. The

dependency of the viscosity ratio was further studied. Compared to isoviscous systems, non-isoviscous fluids systems, both with positive and negative viscosity differences, have a negative effect on droplet capture.

Since in **Chapter 2** we first proposed the simple physical model in which microswimmers interact with the soft penetrable/deformable planar interface, to the work in **Chapters 3** and **Chapter 4**, we keep improving our understanding of the dynamics of microswimmers near a fluid-fluid interface by developing a related physical model and progressively adding new variables and constraints to it. Unlike the dynamics of swimmers in the homogeneous fluid, microswimmers exhibit completely different motions near the fluid-fluid interface. Until now, four motions are observed, namely, "bouncing", "sliding", "penetrating" and "hovering" motion, depending on different factors. These factors are mainly derived from two aspects, particle properties including collision angles, swimming types and strength, and liquid (interface) properties such as viscosity difference and interfacial geometry.

5.2   Future outlooks

Regarding future work, on the one hand, we can continue further research on the full dynamics of swimmers near the interface. More features can be added to the basic model to understand more practical cases in biology. For example, the fluid system in the current work is isodense. In further work, the phase-dependent density function can be introduced to study the motion of microswimmers in fluids with different densities. The swimmer's affinity for different fluids can also be taken into consideration, corresponding to the hydrophilic/hydrophobic of particles. Moreover, in the Deepwater Horizon oil spill in 2010 which we once mentioned in the **Chapter 4**, it's also known that a huge amount of dispersant/surfactant was added at the well head to break down the heavier hydrocarbons into tiny droplets, and aid bioremediation [107]. In order to further investigate the role of the surfactant, the interfacial viscosity and chemical interaction

between the fluid and the particle should also be accounted for, allowing us to study the surfactant dynamics.

On the other hand, as an example of industrial applications of microswimmers, an artificial microrobot for drug-targeted delivery should be more proactive. It can travel along a specific route which is initially set by users, and carry out transmembrane drug transport near the lesion. We hope it will be able to achieve such functions by adjusting particle properties according to the particle's near-field fluid environment as the works in this dissertation can provide a theoretical basis and numerical simulation for this kind of algorithm.

Bibliography

[1] Eskandar Moghimipour, Samaneh Abedishirehjin, Maryam Abedini Baghbadorani, and Somayeh Handali. Bacteria and archaea: A new era of cancer therapy. *Journal of Controlled Release*, 338:1–7, 2021.

[2] Eric Lauga and Raymond E Goldstein. microswimmers. *Phys. Today*, 65(9):30, 2012.

[3] JE Avron, O Kenneth, and DH Oaknin. Pushmepullyou: an efficient microswimmer. *New Journal of Physics*, 7(1):234, 2005.

[4] Jens Elgeti, Roland G Winkler, and Gerhard Gompper. Physics of microswimmers—single particle motion and collective behavior: a review. *Reports on progress in physics*, 78(5):056601, 2015.

[5] Raphaël Jeanneret, Matteo Contino, and Marco Polin. A brief introduction to the model microswimmer chlamydomonas reinhardtii. *The European Physical Journal Special Topics*, 225(11):2141–2156, 2016.

[6] Danni Zhong, Zhen Du, and Min Zhou. Algae: a natural active material for biomedical applications. *View*, 2(4):20200189, 2021.

[7] Julio Bastos-Arrieta, Ainhoa Revilla-Guarinos, William E Uspal, and Juliane Simmchen. Bacterial biohybrid microswimmers. *Frontiers in Robotics and AI*, 5:97, 2018.

[8] PJA Janssen and MD Graham. Coexistence of tight and loose bundled states in a model of bacterial flagellar dynamics. *Physical Review E*, 84(1):011910, 2011.

[9] Howard C Berg. *E. coli in Motion*. Springer, 2004.

[10] Howard C Berg. The rotary motor of bacterial flagella. *Annual review of biochemistry*, 72(1):19–54, 2003.

[11] Benjamin M Friedrich, Ingmar H Riedel-Kruse, Jonathon Howard, and Frank Jülicher. High-precision tracking of sperm swimming fine structure provides strong test of resistive force theory. *Journal of Experimental Biology*, 213(8):1226–1234, 2010.

[12] J Cosson, P Huitorel, and C Gagnon. How spermatozoa come to be confined to surfaces. *Cell motility and the cytoskeleton*, 54(1):56–63, 2003.

[13] DM Woolley. Motility of spermatozoa at surfaces. *REPRODUCTION-CAMBRIDGE-*, 126(2):259–270, 2003.

[14] U Benjamin Kaupp, Johannes Solzin, Eilo Hildebrand, Joel E Brown, Annika Helbig, Volker Hagen, Michael Beyermann, Francesco Pampaloni, and Ingo Weyand. The signal flow and motor response controling chemotaxis of sea urchin sperm. *Nature cell biology*, 5(2):109–117, 2003.

[15] U Benjamin Kaupp, Nachiket D Kashikar, and Ingo Weyand. Mechanisms of sperm chemotaxis. *Annual review of physiology*, 70(1):93–117, 2008.

[16] Michael Eisenbach and Laura C Giojalas. Sperm guidance in mammals—an unpaved road to the egg. *Nature reviews Molecular cell biology*, 7(4):276–285, 2006.

[17] Benjamin M Friedrich and Frank Jülicher. Chemotaxis of sperm cells. *Proceedings of the National Academy of Sciences*, 104(33):13256–13261, 2007.

[18] Luis Alvarez, Benjamin M Friedrich, Gerhard Gompper, and U Benjamin Kaupp. The computational sperm cell. *Trends in cell biology*, 24(3):198–207, 2014.

[19] MM Stanton, C Trichet-Paredes, and Samuel Sanchez. Applications of three-dimensional (3d) printing for microswimmers and bio-hybrid robotics. *Lab on a Chip*, 15(7):1634–1637, 2015.

[20] Xiaopu Wang, Xiao-Hua Qin, Chengzhi Hu, Anastasia Terzopoulou, Xiang-Zhong Chen, Tian-Yun Huang, Katharina Maniura-Weber, Salvador Pané, and Bradley J Nelson. 3d printed enzymatically biodegradable soft helical microswimmers. *Advanced Functional Materials*, 28(45):1804107, 2018.

[21] U Kei Cheang, Dheeraj Roy, Jun Hee Lee, and Min Jun Kim. Fabrication and magnetic control of bacteria-inspired robotic microswimmers. *Applied Physics Letters*, 97(21):213704, 2010.

[22] U Kei Cheang, Kyoungwoo Lee, Anak Agung Julius, and Min Jun Kim. Multiple-robot drug delivery strategy through coordinated teams of microswimmers. *Applied physics letters*, 105(8):083705, 2014.

[23] J Scogna, J Olkowski, N Fatema, P Parameswaran, and V Dhillon. Biologically inspired robotic microswimmers. In *2011 IEEE 37th Annual Northeast Bioengineering Conference (NEBEC)*, pages 1–2. IEEE, 2011.

[24] Naveen Kumar Agrawal, Pallab Sinha Mahapatra, and Tuhin S Santra. Micro-robots/microswimmers for biomedical applications. *Microfluidics and Bio-MEMS*, pages 95–148, 2020.

[25] Immihan Ceren Yasa, Hakan Ceylan, Ugur Bozuyuk, Anna-Maria Wild, and Metin Sitti. Elucidating the interaction dynamics between microswimmer body and immune system for medical microrobots. *Science Robotics*, 5(43):eaaz3867, 2020.

[26] Edward M Purcell. Life at low reynolds number. *American journal of physics*, 45(1):3–11, 1977.

[27] Daniel Ahmed, Cornel Dillinger, Ayoung Hong, and Bradley J Nelson. Artificial acousto-magnetic soft microswimmers. *Advanced Materials Technologies*, 2(7):1700050, 2017.

[28] Klaas Bente, Agnese Codutti, Felix Bachmann, and Damien Faivre. Biohybrid and bioinspired magnetic microswimmers. *Small*, 14(29):1704374, 2018.

[29] Ali Ghanbari, Mohsen Bahrami, and Mohammad RH Nobari. Methodology for artificial microswimming using magnetic actuation. *Physical Review E*, 83(4):046301, 2011.

[30] Baohu Dai, Jizhuang Wang, Ze Xiong, Xiaojun Zhan, Wei Dai, Chien-Cheng Li, Shien-Ping Feng, and Jinyao Tang. Programmable artificial phototactic microswimmer. *Nature nanotechnology*, 11(12):1087–1092, 2016.

[31] Jia Dai, Xiang Cheng, Xiaofeng Li, Zhisheng Wang, Yufeng Wang, Jing Zheng, Jun Liu, Jiawei Chen, Changjin Wu, and Jinyao Tang. Solution-synthesized multifunctional janus nanotree microswimmer. *Advanced Functional Materials*, 31(48):2106204, 2021.

[32] MJ Lighthill. On the squirming motion of nearly spherical deformable bodies through liquids at very small reynolds numbers. *Communications on pure and applied mathematics*, 5(2):109–118, 1952.

[33] John R Blake. A spherical envelope approach to ciliary propulsion. *Journal of Fluid Mechanics*, 46(1):199–208, 1971.

[34] On Shun Pak and Eric Lauga. Generalized squirming motion of a sphere. *Journal of Engineering Mathematics*, 88(1):1–28, 2014.

[35] Takuji Ishikawa, MP Simmonds, and Timothy J Pedley. Hydrodynamic interaction of two swimming model micro-organisms. *Journal of Fluid Mechanics*, 568:119–160, 2006.

[36] Ryoichi Yamamoto, John J Molina, and Yasuya Nakayama. Smoothed profile method for direct numerical simulations of hydrodynamically interacting particles. *Soft Matter*, 17(16):4226–4253, 2021.

[37] Xian Luo, Martin R Maxey, and George Em Karniadakis. Smoothed profile method for particulate flows: Error analysis and simulations. *Journal of Computational Physics*, 228(5):1750–1769, 2009.

[38] Ryoichi Yamamoto, Yasuya Nakayama, and Kang Kim. A smooth interface method for simulating liquid crystal colloid dispersions. *Journal of Physics: Condensed Matter*, 16(19):S1945, 2004.

[39] Yasuya Nakayama and Ryoichi Yamamoto. Simulation method to resolve hydrodynamic interactions in colloidal dispersions. *Phys. Rev. E*, 71:036707, Mar 2005.

[40] John J Molina and Ryoichi Yamamoto. Direct numerical simulations of rigid body dispersions. i. mobility/friction tensors of assemblies of spheres. *The Journal of chemical physics*, 139(23):234105, 2013.

[41] Gregory Lecrivain, Yuki Kotani, Ryoichi Yamamoto, Uwe Hampel, and Takashi Taniguchi. Diffuse interface model to simulate the rise of a fluid droplet across a cloud of particles. *Physical Review Fluids*, 3(9):094002, 2018.

[42] John J. Molina, Kotaro Otomura, Hayato Shiba, Hideki Kobayashi, Masaki Sano, and Ryoichi Yamamoto. Rheological evaluation of colloidal dispersions using the smoothed profile method: Formulation and applications. *Journal of Fluid Mechanics*, 792:590–619, 2016.

[43] Kang Kim, Yasuya Nakayama, and Ryoichi Yamamoto. Direct numerical simulations of electrophoresis of charged colloids. *Physical Review Letters*, 96(20):1–4, 2006.

[44] Nozomi Arai, Satoshi Watanabe, Minoru T Miyahara, Ryoichi Yamamoto, Uwe Hampel, and Gregory Lecrivain. Direct observation of the attachment behavior of hydrophobic colloidal particles onto a bubble surface. *Soft matter*, 16(3):695–702, 2020.

[45] Gregory Lecrivain, Taisa Beatriz Pacheco Grein, Ryoichi Yamamoto, Uwe Hampel, and Takashi Taniguchi. Eulerian/lagrangian formulation for the elasto-capillary deformation of a flexible fibre. *Journal of Computational Physics*, 409:109324, 2020.

[46] Knut Drescher, Raymond E Goldstein, Nicolas Michel, Marco Polin, and Idan Tuval. Direct measurement of the flow field around swimming microorganisms. *Physical Review Letters*, 105(16):168101, 2010.

[47] Eric Lauga. Bacterial hydrodynamics. *Annual Review of Fluid Mechanics*, 48:105–130, 2016.

[48] Damien Laage and James T Hynes. A molecular jump mechanism of water reorientation. *Science*, 311(5762):832–835, 2006.

[49] Hakan Ceylan, Immihan Ceren Yasa, Oncay Yasa, Ahmet Fatih Tabak, Joshua Giltinan, and Metin Sitti. 3d-printed biodegradable microswimmer for theranostic cargo delivery and release. *ACS Nano*, 13(3):3353–3362, February 2019.

[50] Matthew T Downton and Holger Stark. Simulation of a model microswimmer. *Journal of Physics: Condensed Matter*, 21(20):204101, 2009.

[51] Giorgio Volpe, Sylvain Gigan, and Giovanni Volpe. Simulation of the active brownian motion of a microswimmer. *American Journal of Physics*, 82(7):659–664, 2014.

[52] Norihiro Oyama, John Jairo Molina, and Ryoichi Yamamoto. Purely hydrodynamic origin for swarming of swimming particles. *Physical Review E*, 93(4):043114, 2016.

[53] Giovanni Volpe, Ivo Buttinoni, Dominik Vogt, Hans-Jürgen Kümmerer, and Clemens Bechinger. Microswimmers in patterned environments. *Soft Matter*, 7(19):8810–8815, 2011.

[54] Gao-Jin Li and Arezoo M Ardekani. Hydrodynamic interaction of microswimmers near a wall. *Physical Review E*, 90(1):013010, 2014.

[55] Kenta Ishimoto and Darren G Crowdy. Dynamics of a treadmilling microswimmer near a no-slip wall in simple shear. *Journal of Fluid Mechanics*, 821:647–667, 2017.

[56] Federico Fadda, John Jairo Molina, and Ryoichi Yamamoto. Dynamics of a chiral swimmer sedimenting on a flat plate. *Physical Review E*, 101(5):052608, 2020.

[57] Kenta Ishimoto and Eamonn A Gaffney. Squirmer dynamics near a boundary. *Physical Review E*, 88(6):062702, 2013.

[58] Vaseem A Shaik and Arezoo M Ardekani. Motion of a model swimmer near a weakly deforming interface. *Journal of Fluid Mechanics*, 824:42–73, 2017.

[59] Abdallah Daddi-Moussa-Ider, Christina Kurzthaler, Christian Hoell, Andreas Zöttl, Mehdi Mirzakhanloo, Mohammad-Reza Alam, Andreas M Menzel, Hartmut Löwen, and Stephan Gekle. Frequency-dependent higher-order stokes singularities near a planar elastic boundary: Implications for the hydrodynamics of an active microswimmer near an elastic interface. *Physical Review E*, 100(3):032610, 2019.

[60] See supplemental material at `https://sm.cheme.kyoto-u.ac.jp/supplementary-movies/`.

[61] Bum Jun Park, Teresa Brugarolas, and Daeyeon Lee. Janus particles at an oil–water interface. *Soft Matter*, 7(14):6413–6417, 2011.

[62] Daniela Pimponi, Mauro Chinappi, Paolo Gualtieri, and Carlo Massimo Casciola. Hydrodynamics of flagellated microswimmers near free-slip interfaces. *Journal of Fluid Mechanics*, 789:514–533, 2016.

[63] Harinadha Gidituri, Zaiyi Shen, Alois Würger, and Juho S Lintuvuori. Reorientation dynamics of microswimmers at fluid-fluid interfaces. *Physical Review Fluids*, 7(4):L042001, 2022.

[64] Jiayi Deng, Mehdi Molaei, Nicholas G Chisholm, and Kathleen J Stebe. Motile bacteria at oil–water interfaces: Pseudomonas aeruginosa. *Langmuir*, 36(25):6888–6902, 2020.

[65] Nikhil Desai and Arezoo M Ardekani. Biofilms at interfaces: microbial distribution in floating films. *Soft Matter*, 16(7):1731–1750, 2020.

[66] Gerhard Gompper, Clemens Bechinger, Stephan Herminghaus, Rolf Isele-Holder, U Benjamin Kaupp, Hartmut Löwen, Holger Stark, and Roland G Winkler. Microswimmers–from single particle motion to collective behavior, 2016.

[67] https://kapsel-dns.com.

[68] Jackson C Kirkman-Brown and David J Smith. Sperm motility: is viscosity fundamental to progress? *MHR: Basic science of reproductive medicine*, 17(8):539–544, 2011.

[69] H Gadêlha, EA Gaffney, DJ Smith, and JC Kirkman-Brown. Nonlinear instability in flagellar dynamics: a novel modulation mechanism in sperm migration? *Journal of The Royal Society Interface*, 7(53):1689–1697, 2010.

[70] Lars Björndahl. The usefulness and significance of assessing rapidly progressive spermatozoa. *Asian Journal of Andrology*, 12(1):33, 2010.

[71] Hung V Nguyen and Vincent Faivre. Targeted drug delivery therapies inspired by natural taxes. *Journal of Controlled Release*, 322:439–456, 2020.

[72] Babak Mostaghaci, Oncay Yasa, Jiang Zhuang, and Metin Sitti. Bioadhesive bacterial microswimmers for targeted drug delivery in the urinary and gastrointestinal tracts. *Advanced Science*, 4(6):1700058, 2017.

[73] Byung-Wook Park, Jiang Zhuang, Oncay Yasa, and Metin Sitti. Multifunctional bacteria-driven microswimmers for targeted active drug delivery. *ACS nano*, 11(9):8910–8923, 2017.

[74] Xiaohui Yan, Qi Zhou, Jiangfan Yu, Tiantian Xu, Yan Deng, Tao Tang, Qian Feng, Liming Bian, Yan Zhang, Antoine Ferreira, et al. Magnetite nanostructured porous hollow helical microswimmers for targeted delivery. *Advanced Functional Materials*, 25(33):5333–5342, 2015.

[75] Juho S Lintuvuori, Aidan T Brown, Kevin Stratford, and Davide Marenduzzo. Hydrodynamic oscillations and variable swimming speed in squirmers close to repulsive walls. *Soft Matter*, 12(38):7959–7968, 2016.

[76] Ignacio Pagonabarraga and Isaac Llopis. The structure and rheology of sheared model swimmer suspensions. *Soft Matter*, 9(29):7174–7184, 2013.

[77] Zaiyi Shen, Alois Würger, and Juho S Lintuvuori. Hydrodynamic interaction of a self-propelling particle with a wall. *The European Physical Journal E*, 41(3):1–9, 2018.

[78] Eric Lauga, Willow R DiLuzio, George M Whitesides, and Howard A Stone. Swimming in circles: motion of bacteria near solid boundaries. *Biophysical journal*, 90(2):400–412, 2006.

[79] T Peter, P Malgaretti, Nicolas Rivas, A Scagliarini, J Harting, and S Dietrich. Numerical simulations of self-diffusiophoretic colloids at fluid interfaces. *Soft Matter*, 16(14):3536–3547, 2020.

[80] R Di Leonardo, D Dell'Arciprete, L Angelani, and V Iebba. Swimming with an image. *Physical review letters*, 106(3):038101, 2011.

[81] Xiaolu Wang, Martin In, Christophe Blanc, Paolo Malgaretti, Maurizio Nobili, and Antonio Stocco. Wetting and orientation of catalytic janus colloids at the surface of water. *Faraday discussions*, 191:305–324, 2016.

[82] P Malgaretti, MN Popescu, and S Dietrich. Self-diffusiophoresis induced by fluid interfaces. *Soft Matter*, 14(8):1375–1388, 2018.

[83] Paolo Malgaretti and Jens Harting. Phoretic colloids close to and trapped at fluid interfaces. *ChemNanoMat*, 7(10):1073–1081, 2021.

[84] Eamonn A Gaffney, Hermes Gadêlha, David J Smith, John R Blake, and Jackson C Kirkman-Brown. Mammalian sperm motility: observation and theory. *Annual Review of Fluid Mechanics*, 2011.

[85] Chao Feng, John J. Molina, Matthew S. Turner, and Ryoichi Yamamoto. Dynamics of microswimmers near a soft penetrable interface. *Phys. Rev. Res.*, 4:043202, Dec 2022.

[86] Charu Datt and Gwynn J Elfring. Active particles in viscosity gradients. *Physical Review Letters*, 123(15):158006, 2019.

[87] Benno Liebchen, Paul Monderkamp, Borge Ten Hagen, and Hartmut Löwen. Viscotaxis: Microswimmer navigation in viscosity gradients. *Physical review letters*, 120(20):208002, 2018.

[88] Rajat Dandekar and Arezoo M Ardekani. Swimming sheet in a viscosity-stratified fluid. *Journal of Fluid Mechanics*, 895, 2020.

[89] Patrick S Eastham and Kourosh Shoele. Axisymmetric squirmers in stokes fluid with nonuniform viscosity. *Physical Review Fluids*, 5(6):063102, 2020.

[90] Michael J Daniels, Jane M Longland, and James Gilbart. Aspects of motility and chemotaxis in spiroplasmas. *Microbiology*, 118(2):429–436, 1980.

[91] Kyosuke Takabe, Hajime Tahara, Md Shafiqul Islam, Samia Affroze, Seishi Kudo, and Shuichi Nakamura. Viscosity-dependent variations in the cell shape and swimming manner of leptospira. *Microbiology*, 163(2):153–160, 2017.

[92] Simone Coppola and Vasily Kantsler. Green algae scatter off sharp viscosity gradients. *Scientific reports*, 11(1):1–7, 2021.

[93] Michael R Stehnach, Nicolas Waisbord, Derek M Walkama, and Jeffrey S Guasto. Viscophobic turning dictates microalgae transport in viscosity gradients. *Nature Physics*, 17(8):926–930, 2021.

[94] Christian Esparza López, Jorge Gonzalez-Gutierrez, Francisco Solorio-Ordaz, Eric Lauga, and Roberto Zenit. Dynamics of a helical swimmer crossing viscosity gradients. *Physical Review Fluids*, 6(8):083102, 2021.

[95] George O'Toole, Heidi B Kaplan, and Roberto Kolter. Biofilm formation as microbial development. *Annual review of microbiology*, 54:49, 2000.

[96] Thomas Danhorn and Clay Fuqua. Biofilm formation by plant-associated bacteria. *Annu. Rev. Microbiol.*, 61:401–422, 2007.

[97] A Karimi, D Karig, A Kumar, and AM Ardekani. Interplay of physical mechanisms and biofilm processes: review of microfluidic methods. *Lab on a Chip*, 15(1):23–42, 2015.

[98] Walter F Paxton, Kevin C Kistler, Christine C Olmeda, Ayusman Sen, Sarah K St. Angelo, Yanyan Cao, Thomas E Mallouk, Paul E Lammert, and Vincent H Crespi. Catalytic nanomotors: autonomous movement of striped nanorods. *Journal of the American Chemical Society*, 126(41):13424–13431, 2004.

[99] Rémi Dreyfus, Jean Baudry, Marcus L Roper, Marc Fermigier, Howard A Stone, and Jérôme Bibette. Microscopic artificial swimmers. *Nature*, 437(7060):862–865, 2005.

[100] Jonathan R Howse, Richard AL Jones, Anthony J Ryan, Tim Gough, Reza Vafabakhsh, and Ramin Golestanian. Self-motile colloidal particles: from directed propulsion to random walk. *Physical review letters*, 99(4):048102, 2007.

[101] Ambarish Ghosh and Peer Fischer. Controlled propulsion of artificial magnetic nanostructured propellers. *Nano letters*, 9(6):2243–2245, 2009.

[102] Daisuke Takagi, Jérémie Palacci, Adam B Braunschweig, Michael J Shelley, and Jun Zhang. Hydrodynamic capture of microswimmers into sphere-bound orbits. *Soft Matter*, 10(11):1784–1789, 2014.

[103] Juliane Simmchen, Jaideep Katuri, William E Uspal, Mihail N Popescu, Mykola Tasinkevych, and Samuel Sánchez. Topographical pathways guide chemical microswimmers. *Nature communications*, 7(1):1–9, 2016.

[104] Nikhil Desai, Vaseem A Shaik, and Arezoo M Ardekani. Hydrodynamics-mediated trapping of micro-swimmers near drops. *Soft matter*, 14(2):264–278, 2018.

[105] Saverio E Spagnolie, Gregorio R Moreno-Flores, Denis Bartolo, and Eric Lauga. Geometric capture and escape of a microswimmer colliding with an obstacle. *Soft Matter*, 11(17):3396–3411, 2015.

[106] Ian M Head, D Martin Jones, and Wilfred FM Röling. Marine microorganisms make a meal of oil. *Nature Reviews Microbiology*, 4(3):173–182, 2006.

[107] Ronald M Atlas and Terry C Hazen. Oil biodegradation and bioremediation: a tale of the two worst spills in us history, 2011.

[108] Christopher M Reddy, J Samuel Arey, Jeffrey S Seewald, Sean P Sylva, Karin L Lemkau, Robert K Nelson, Catherine A Carmichael, Cameron P McIntyre, Judith Fenwick, G Todd Ventura, et al. Composition and fate of gas and oil released to the water column during the deepwater horizon oil spill. *Proceedings of the National Academy of Sciences*, 109(50):20229–20234, 2012.

[109] Terry C Hazen, Eric A Dubinsky, Todd Z DeSantis, Gary L Andersen, Yvette M Piceno, Navjeet Singh, Janet K Jansson, Alexander Probst, Sharon E Borglin, Julian L Fortney, et al. Deep-sea oil plume enriches indigenous oil-degrading bacteria. *Science*, 330(6001):204–208, 2010.

[110] David L Valentine, John D Kessler, Molly C Redmond, Stephanie D Mendes, Monica B Heintz, Christopher Farwell, Lei Hu, Franklin S Kinnaman, Shari Yvon-Lewis, Mengran Du, et al. Propane respiration jump-starts microbial response to a deep oil spill. *Science*, 330(6001):208–211, 2010.

[111] John D Kessler, David L Valentine, Molly C Redmond, Mengran Du, Eric W Chan, Stephanie D Mendes, Erik W Quiroz, Christie J Villanueva, Stephani S Shusta, Lindsay M Werra, et al. A persistent oxygen anomaly reveals the fate of spilled methane in the deep gulf of mexico. *Science*, 331(6015):312–315, 2011.

[112] Łukasz Ławniczak, Marta Woźniak-Karczewska, Andreas P Loibner, Hermann J Heipieper, and Łukasz Chrzanowski. Microbial degradation of hydrocarbons—basic principles for bioremediation: a review. *Molecules*, 25(4):856, 2020.

[113] Santanu Paria. Surfactant-enhanced remediation of organic contaminated soil and water. *Advances in colloid and interface science*, 138(1):24–58, 2008.